CANCER
COMMUNICATIONS Open Access

ORIGINAL ARTICLE

Snail acetylation by autophagy-derived acetyl-coenzyme A promotes invasion and metastasis of *KRAS-LKB1* co-mutated lung cancer cells

Jang Hee Han[1,2,3]   Yong Keon Kim[1,7]   Hakhyun Kim[1,7]   Jooyoung Lee[1,4]
Myung Joon Oh[1,7]   Sang Bum Kim[1]   Minjee Kim[1,7]   Kook Hwan Kim[1]
Hyun Ju Yoon[1,7]   Myung-Shik Lee[1]   John D. Minna[5]   Michael A. White[6]
Hyun Seok Kim[1,4,7] ⓘ

[1]Severance Biomedical Science Institute, Yonsei University College of Medicine, Seoul 03722, Korea

[2]Department of Medical Science, Yonsei University Graduate School, Seoul 03722, Korea

[3]Department of Urology, Seoul National University Hospital, Seoul 03722, Korea

[4]Checkmate Therapeutics Inc., Seoul 07207, Korea

[5]Hamon Center for Therapeutic Oncology Research, University of Texas Southwestern Medical Center, Dallas, Texas 75390, USA

[6]Department of Cell Biology, University of Texas Southwestern Medical Center, Dallas, Texas 75390, USA

[7]Graduate School of Medical Science, Brain Korea 21 Project, Yonsei University College of Medicine, Seoul 03722, Korea

Correspondence
Hyun Seok Kim, Severance Biomedical Science Institute, Yonsei University College of Medicine, Seoul 03722, Korea.
Email: hsfkim@yuhs.ac

Abstract

Background: Autophagy is elevated in metastatic tumors and is often associated with active epithelial-to-mesenchymal transition (EMT). However, the extent to which EMT is dependent on autophagy is largely unknown. This study aimed to identify the mechanisms by which autophagy facilitates EMT.

Methods: We employed a liquid chromatography-based metabolomic approach with kirsten rat sarcoma viral oncogene (*KRAS*) and liver kinase B1 (*LKB1*) gene co-mutated (KL) cells that represent an autophagy/EMT-coactivated invasive lung cancer subtype for the identification of metabolites linked to

Abbreviations: ACACA, Acetyl-CoA carboxylase alpha; ACLY, ATP citrate lyase; ACSS2, Acyl-CoA synthetase short chain family member 2; AMPK, AMP-activated protein kinase; ATG5, autophagy related 5; CAMKK2, calcium/calmodulin-dependent protein kinase kinase 2; CBP, CREB-binding protein; CCLE, Cancer Cell Line Encyclopedia; CHX, cycloheximide; CLEAR, coordinated lysosomal expression and regulation; CPTAC, Clinical Proteomic Tumor Analysis Consortium; CQ, chloroquine; EMT, epithelial-mesenchymal transition; HDAC, histone deacetylase; HSP90, Heat shock protein 90; IP, immunoprecipitation; LAMP2, lysosomal Associated Membrane Protein 2; LC3B, Microtubule-associated protein 1A/1B-light chain 3; MOG, dimethyl-2-oxoglutarate; MP, methyl pyruvate; NAC, N-acetyl cysteine; NRF2, NF-E2-related factor 2; ROS, reactive oxygen species; Rosi, rosiglitazone; ssGSEA, single sample Gene Set Enrichment analysis; TFEB, transcription factor EB; ULK1, Unc-51-like kinase.

Yong Keon Kim and Hakhyun Kim contributed equally to this work.

- -

autophagy-driven EMT activation. Molecular mechanisms of autophagy-driven EMT activation were further investigated by quantitative real-time polymerase chain reaction (qRT-PCR), Western blotting analysis, immunoprecipitation, immunofluorescence staining, and metabolite assays. The effects of chemical and genetic perturbations on autophagic flux were assessed by two orthogonal approaches: microtubule-associated protein 1A/1B-light chain 3 (LC3) turnover analysis by Western blotting and monomeric red fluorescent protein-green fluorescent protein (mRFP-GFP)-LC3 tandem fluorescent protein quenching assay. Transcription factor EB (TFEB) activity was measured by coordinated lysosomal expression and regulation (CLEAR) motif-driven luciferase reporter assay. Experimental metastasis (tail vein injection) mouse models were used to evaluate the impact of calcium/calmodulin-dependent protein kinase kinase 2 (CAMKK2) or ATP citrate lyase (ACLY) inhibitors on lung metastasis using IVIS luciferase imaging system.

Results: We found that autophagy in KL cancer cells increased acetyl-coenzyme A (acetyl-CoA), which facilitated the acetylation and stabilization of the EMT-inducing transcription factor Snail. The autophagy/acetyl-CoA/acetyl-Snail axis was further validated in tumor tissues and in autophagy-activated pancreatic cancer cells. TFEB acetylation in KL cancer cells sustained pro-metastatic autophagy in a mammalian target of rapamycin complex 1 (mTORC1)-independent manner. Pharmacological inhibition of this axis via CAMKK2 inhibitors or ACLY inhibitors consistently reduced the metastatic capacity of KL cancer cells in vivo.

Conclusions: This study demonstrates that autophagy-derived acetyl-CoA promotes Snail acetylation and thereby facilitates invasion and metastasis of *KRAS-LKB1* co-mutated lung cancer cells and that inhibition of the autophagy/acetyl-CoA/acetyl-Snail axis using CAMKK2 or ACLY inhibitors could be a potential therapeutic strategy to suppress metastasis of KL lung cancer.

KEYWORDS

snail, autophagy, acetyl-coenzyme A, epithelial-to-mesenchymal transition, non-small-cell lung cancer, CAMKK2, acetyl-snail, pancreatic cancer, KRAS inhibitor, metastasis, ACLY

1 | BACKGROUND

Lung cancer is the leading cause of cancer death worldwide, and its low survival rate is because approximately 80% of patients are initially diagnosed with regional or distant metastasis [1, 2]. *KRAS*-mutated non-small cell lung cancer (NSCLC) exhibits heterogeneous biological characteristics and different therapeutic responses depending on the accompanying co-mutations with other genes (e.g., tumor protein p53 (*TP53*), liver kinase B1 (*STK11/LKB1*, hereafter *LKB1*), kelch like ECH associated protein 1 (*KEAP1*), cyclin dependent kinase inhibitor 2A/2B (*CDKN2A/CDKN2B*) [3–6]. Specifically, patients harbor-

ing mutations in *KRAS* and the tumor suppressor gene *LKB1*, two commonly mutated genes in NSCLC, develop aggressive lung tumors, show a high frequency of metastasis and are refractory to the currently available therapies [7, 8]. In our previous study, we found that *KRAS-LKB1* co-mutated (KL) NSCLC cells displayed epithelial-to-mesenchymal transition (EMT)-like molecular signatures and exhibited highly elevated lysosomal/autophagosome-lysosomal function [4]. EMT is required for the initiation of metastasis by changing adherent epithelial cancer cells into highly motile mesenchymal cells, thereby facilitating invasion and metastasis [9]. Macroautophagy (autophagy hereafter) is a lysosome-mediated catabolic process

elevated in metastatic tumors and is often associated with active EMT [10]. However, the extent to which EMT is dependent on autophagy and the mechanism by which autophagy facilitates EMT are largely unknown.

In the present study, we sought to dissect the mechanisms of autophagic activation in KL lung cancer cells and the mechanisms by which autophagy enhances EMT and invasion in this aggressive tumor subtype.

2 | MATERIALS AND METHODS

2.1 | Cell lines and cell culture

HBEC30KT cells are normal human bronchial epithelial cells immortalized with cyclin dependent kinase 4 (*CDK4*) and human telomerase reverse transcriptase (*hTERT*). HBEC30KT-derived cancer progression cell lines (HBEC30KT, abbreviated as hb30; HBEC30KT-shTP53, abbreviated as hb30-P; HBEC30KT-shTP53/KRAS G12V, abbreviated as hb30-KP; and HBEC30KT-shTP53/KRAS G12V/shLKB1, abbreviated as hb30-KPL) were generated as previously described [4]. Adenocarcinoma of lung-4 (ACL4) [RPMI-1640 medium (11875-093, Gibco, Waltham, MA, USA), 2.05 mmol/L L-glutamine supplemented with 0.02 mg/mL insulin, 0.01 mg/mL transferrin, 25 nmol/L sodium selenite, 50 nmol/L hydrocortisone, 10 mmol/L hydroxyethyl piperazine ethane sulfonic acid (HEPES), 1 ng/mL epidermal growth factor (EGF), 0.01 mmol/L ethanolamine, 0.01 mmol/L O-phosphorylethanolamine, 0.1 nmol/L triiodothyronine, 2 mg/mL bovine serum albumin (BSA), and 0.5 mmol/L sodium pyruvate] supplemented with 2% fetal bovine serum (16000-044, Gibco) and 1% penicillin-streptomycin (15140122, Gibco) was used to culture the HBEC30KT progression series at 37°C with 5% CO_2. All NSCLC cell lines used in this study, except the human lung squamous cell carcinoma cell line Calu-1, which were purchased from the Korean Cell Line Bank (Seoul, Korea), were established by our laboratory at the National Cancer Institute (NCI) and Hamon Center for Therapeutic Oncology Research (Dallas, TX, USA) [11]. For pancreatic cancer cell lines, the human pancreatic ductal adenocarcinoma cell line Panc-1 was purchased from the Korean Cell Line Bank, and human pancreatic ducal adenocarcinoma cell lines KP4, KP4-1, and PK-59 were purchased from Riken (Tsukuba, Japan). NSCLC cell lines and pancreatic cancer cell lines were maintained in RPMI-1640 medium supplemented with 5% (v/v) and 10% (v/v) fetal bovine serum, respectively, and 1% penicillin-streptomycin at 37°C in 5% CO_2. The luciferase-expressing human lung adenocarcinoma cell line A549-luc (#JCRB1414) was obtained from the Japanese Collection of Research Bioresources Cell Bank (Tokyo, Japan). The

A549-luc cell line was maintained in minimum essential medium (MEM) alpha (12561-056, Gibco) supplemented with 10% (v/v) fetal bovine serum and 1% penicillin-streptomycin at 37°C in 5% CO_2. All cell lines were DNA fingerprinted (PowerPlex 1.2 Kit, Promega, Madison, WI, USA) and mycoplasma-free (e-Myco Kit, Boca Scientific, Dedham, MA, USA). The *KRAS* G12C and *LKB1* mutation statuses of the 11 NSCLC cell lines (A549, NCI-H157, NCI-H460, NCI-H647, HCC44, NCI-H2030, NCI-H2122, NCI-H1155, NCI-H358, NCI-H441, HCC461, Calu-1, NCI-H1373 and HCC1171) used in this study are described in Supplementary Table S1. We performed short tandem repeat-based cell line authentication for cell lines used in this study. Cell line authentication results are provided in Supplementary Table S2.

2.2 | Western blotting

Cells were harvested, washed with phosphate-buffered saline (PBS) and lysed on ice with radioimmunoprecipitation assay buffer (R0278, Sigma, Burlington, MA, USA) containing a protease and phosphatase inhibitor cocktail (GenDEPOT) for 15 min. Then, the cell lysates were centrifuged at 4°C for 10 min at 15,000 rpm. Protein concentrations were measured by a Bradford assay (500-0006, Bio-Rad, Hercules, CA, USA). Equal amounts of total protein were subjected to sodium dodecyl sulfate (SDS) gel electrophoresis and transferred to polyvinylidene difluoride (PVDF) membranes (Bio-Rad). Membranes were blocked with 5% skim milk for 1 h at 25°C and incubated overnight at 4°C with a primary antibody against target protein in buffer containing 0.1% Tween 20. Subsequently, the membranes were washed three times with Tween-PBS buffer and incubated with secondary antibody (anti-rabbit IgG or anti-mouse IgG) diluted in blocking buffer containing 0.1% Tween 20 for 1 hour at 25°C. The membranes were subsequently washed three times with Tween-TBS for 10 min each time. Signals of immunoreactive bands were visualized with a Pierce enhanced chemiluminescence (ECL) Western blotting substrate (32106, Thermo Fisher Scientific, Waltham, MA, USA) or SuperSignal West Pico PLUS chemiluminescent substrate (34578, Thermo Fisher Scientific). The relative abundance of individual proteins was measured by quantifying the intensities of individual protein bands on the Western blots (relative to beta-actin or heat shock protein 90 [HSP90]) using ImageJ software (Bethesda, MD, USA). The following antibodies were used at a 1:1000 dilution: rabbit monoclonal anti-acetyl-CoA carboxylase 1 (ACC1) (#3676, Cell Signaling Technology, Danvers, MA, USA, RRID: AB_2219397), rabbit monoclonal anti-Snail (#3879, Cell Signaling Technology, RRID: AB_2255011), mouse monoclonal anti-Snail (#3895, Cell

Signaling Technology, RRID: AB_2191759), rabbit polyclonal anti-acetyl-histone H3 (#06-599, Millipore, RRID: AB_2115283), rabbit monoclonal anti-S6 (#2217, Cell Signaling Technology, RRID: AB_331355), rabbit monoclonal anti-phospho-S6 (Ser235/236) (#4857, Cell Signaling Technology, RRID: AB_2181035), rabbit polyclonal anti-AMP-activated catalytic subunit alpha 1 (AMPK) (#2532, Cell Signaling Technology, RRID: AB_330331), rabbit monoclonal anti-transcription factor EB (TFEB) (#37785, Cell Signaling Technology, RRID: AB_2799119), mouse monoclonal anti-p53 (#48818, Cell Signaling Technology, RRID: AB_2713958), mouse monoclonal anti-KRAS (#sc-30, Santa Cruz, Santa Cruz, CA, USA, RRID: AB_627865), rabbit monoclonal anti-LKB1 (#3047, Cell Signaling Technology, RRID: AB_2198327), mouse monoclonal anti-phospho-glycogen synthase kinase 3 beta (GSK3β) (Y216) (#612313, BD Biosciences, San Jose, CA, USA, RRID: AB_399628), rabbit monoclonal anti-GSK3β (#9315, Cell Signaling Technology, RRID: AB_490890), rabbit monoclonal anti-Slug (#9585, Cell Signaling Technology, RRID: AB_2239535), rabbit monoclonal anti-zinc finger E-box-binding homeobox 1 (ZEB1) (#3396, Cell Signaling Technology, RRID: AB_1904164), mouse monoclonal anti-Twist1 (#ab50887, Abcam, Cambridge, UK, RRID: AB_883294), rabbit monoclonal anti-phospho-mitogen activated protein kinase kinase 1/2 (MEK1/2) (Ser217/221) (#9154, Cell Signaling Technology, RRID: AB_2138017), rabbit polyclonal anti-MEK1/2 (#9122, Cell Signaling Technology, RRID: AB_823567), mouse monoclonal anti-calcium/calmodulin-dependent protein kinase kinase 2 (CAMKKβ) (#sc-271674, Santa Cruz, RRID: AB_10708844), rabbit monoclonal anti-E-cadherin (#3195, Cell Signaling Technology, RRID: AB_2291471), rabbit monoclonal anti-phospho-AMPK (Thr172) (#2535, Cell Signaling Technology, RRID: AB_331250), rabbit monoclonal anti-phospho-calcium/calmodulin-dependent protein kinase II (CAMKII) (Thr286) (#12716, Cell Signaling Technology, RRID: AB_2713889), rabbit monoclonal anti-NFE2-like BZIP transcription factor 2 (NRF2) (#12721, Cell Signaling Technology, RRID: AB_2715528), rabbit polyclonal anti-unc-51 like autophagy activating kinase 1 (ULK1) (#4773, Cell Signaling Technology, RRID: AB_2288252), rabbit monoclonal K48-polyubiquitin (#8081, Cell Signaling Technology, RRID: AB_10859893), rabbit monoclonal non-phospho-beta-catenin (Ser33/37/Thr41) (#8814, Cell Signaling Technology, RRID: AB_11127203), rabbit polyclonal anti-acetyl-lysine (#9441, Cell Signaling Technology, RRID: AB_331805), rabbit polyclonal anti-acetyl-lysine (#ab80178, Abcam, RRID: AB_1640674), mouse monoclonal anti-phosphoserine/threonine (#612549, BD Biosciences, RRID: AB_399844), rabbit monoclonal anti-ATP citrate lyase (ACLY) (#13390, Cell Signaling Technology, RRID: AB_2798203), rabbit monoclonal anti-CREB-binding protein (CBP) (#7389, Cell Signaling Technology, RRID: AB_2616020), rabbit monoclonal anti-sequestosome 1 (SQSTM1)/p62 (#8025, Cell Signaling Technology, RRID: AB_10859911), rabbit monoclonal anti-phospho-ULK1 (Ser555) (#5869, Cell Signaling Technology, RRID: AB_10707365), rabbit polyclonal anti-autophagy related 5 (ATG5) (#2630, Cell Signaling Technology, RRID: AB_2062340), rabbit monoclonal anti-citrate synthase (CS) (#14309, Cell Signaling Technology, RRID: AB_2665545), rabbit monoclonal anti-isocitrate dehydrogenase 1 (IDH1) (#8137, Cell Signaling Technology, RRID: AB_10950504), rabbit monoclonal anti-phospho-TFEB (Ser211) (#37681, Cell Signaling Technology, RRID: AB_2799117), anti-phospho-p62 (S351) [gift from Dr. Sue Goo Rhee (Yonsei University, Korea) and Masaaki Komatsu (Juntendo University, Japan)] and mouse monoclonal anti-hemagglutinin (HA)-tag (#2367, Cell Signaling Technology, RRID: AB_10691311). Rabbit monoclonal anti-heat shock protein 90 (HSP90) (#4877, Cell Signaling Technology, RRID: AB_2233307), mouse monoclonal anti-β-actin (#sc-47778, Santa Cruz, RRID: AB_2714189), rabbit monoclonal anti-microtubule-associated protein 1 light chain 3 alpha (LC3) (#3868, Cell Signaling Technology, RRID: AB_2137707), rabbit monoclonal anti-Vimentin (#5741, Cell Signaling Technology, RRID: AB_10695459) were used at a 1:3000 dilution. Anti-rabbit IgG (#111-035-144, Jackson ImmunoResearch, West Grove, PA, USA, RRID: AB_2307391) and anti-mouse IgG (#115-035-146, Jackson ImmunoResearch, RRID: AB_2307392) were used at a 1:3000 dilution.

2.3 | Cell treatments

All cell lines were incubated at 37°C and maintained in an atmosphere containing 5% CO_2. For inhibition of autophagy, cells were treated with 50 μmol/L chloroquine (CQ) (C6628, Sigma) or water for 12-24 h. For activation of autophagy, cells were treated with 2 μmol/L rapamycin (S1039, Selleck Chemicals, Houston, TX, USA) or dimethyl sulfoxide (DMSO) for 5 h. Intracellular reactive oxygen species (ROS) levels were modulated by treatment with 10 mmol/L n-acetyl cysteine (NAC) (A7250, Sigma), a hydrogen peroxide solution (100-200 μmol/L) (216763, Sigma) or water, or the NRF2 activator bardoxolone methyl (CDDO-ME) (50 or 100 nmol/L) (S8078, Selleck Chemicals) or DMSO for 4-24 h. Intracellular calcium signaling was modulated by treatment with 20 μmol/L 1,2-bis(2-aminophenoxy)ethane-N,N,N',N'-tetraacetic acid tetrakis(acetoxymethyl) ester (BAPTA-AM) (A1076, Sigma), 2.5 μmol/L calmidazolium chloride (C3930, Sigma) or DMSO for 1 h. Cells were treated with the CBP/p300 inhibitor C646 (25 μmol/L, SML0002, Sigma),

the histone deacetylase (HDAC) inhibitor suberoylanilide hydroxamic acid (SAHA) (3 μmol/L, S1047, Selleck Chemicals), or DMSO for 18-24 h to modulate Snail protein acetylation. The GSK3β inhibitor CHIR-99021 (3 μmol/L, SML1046, Sigma) or DMSO was added for 24 h to modulate Snail protein phosphorylation. Cells were treated with 1 μmol/L FK506 (S5003, Selleck Chemicals) or DMSO for 1 h to modulate TFEB protein phosphorylation. For nutrient supplementation, cells were treated with 10 mmol/L sodium acetate (S2889, Sigma), 8 mmol/L methyl pyruvate (371173, Sigma), or 3 mmol/L dimethyl 2-oxoglutarate (349631, Sigma) for 24 h. For ACLY inhibition, cells were treated with ACLY inhibitors BMS-303141 (50 μmol/L, S0277, Selleck Chemicals), NDI-091143 (1 μmol/L, S8878, Selleck Chemicals), and SB-204990 (10 and 20 μmol/L, 15245, Cayman, Ann Arbor, MI, USA) for 24 h, 24 h, and 2 h, respectively, or with DMSO as a counterpart. For proteasomal inhibition, cells were co-treated with 20 nmol/L bortezomib (proteasome inhibitor) (S1013, Selleck Chemicals) for the last 3-4 h of assay after treatment with CQ, STO-609, or BMS-303141. For promotion of mitochondrial biogenesis, cells were treated with the peroxisome proliferator-activated receptor gamma (PPARγ) agonist rosiglitazone (200 μmol/L, S2556, Selleck Chemicals) or DMSO for 24 h. For CAMKK2 inhibition, cells were treated with the CAMKK2 inhibitor STO-609 (25 and 50 μmol/L) (S1318, Sigma) or DMSO for 24 h. For KRAS G12C inhibition, cells were treated with the KRAS G12C inhibitor AMG-510 (100 nmol/L or 1 μmol/L, 8830, Selleck Chemicals) or DMSO for 48 h.

For small interfering RNA (siRNA) treatment, cells were transfected with different siRNAs purchased from Genolution (Seoul, Korea) at concentrations of 40–50 nmol/L with Lipofectamine RNAiMAX (13778150, Thermo Fisher Scientific) and were used for different experiments after 48–72 h. All siRNA experiments were performed by pooling three to four siRNAs of each gene as specified in Supplementary Table S3. For the cDNA plasmid transfection assay, cells were transfected with 1–2 μg of different expression vectors in 6-well plates with Lipofectamine 2000 (11668019, Thermo Fisher Scientific) and were used for different experiments after 24 h. Validation of the siRNA and expression vector efficiency was performed by Western blotting of the target protein. siRNA and cDNA sequences are listed in Supplementary Table S3.

2.4 | Construction of plasmids

pGL4.70 5× CLEAR Renilla luciferase (Rluc) vectors were constructed by inserting fragments with 5× repeated coordinated lysosomal expression and regulation (CLEAR) and CMVmini promoter sequences into NheI/XhoI-digested pGL4.70-Rluc vectors (E6881, Promega). For generation of Lenti-5× CLEAR Rluc-CMV-mCherry-T2A-Puro vectors, 3-phosphoglycerate kinase-green fluorescent protein (PGK-GFP) and elongation factor-1 alpha-multiple cloning site (EF1-MCS) fragments of pCDH-EF1-MCS-PGK-GFP-T2A-Puro vectors (CD813A-1, System Biosciences, Palo Alto, CA, USA) were linked with AgeI/NruI-digested CMV-mCherry and ClaI/NotI-digested MCS-Rluc fragments, respectively. Then, Lenti-5× CLEAR Rluc-CMV-mCherry-T2A-Puro vectors were constructed by inserting 5× CLEAR fragments into NheI/XhoI-digested pCDH-MCS-Rluc-CMV-mCherry-T2A-Puro vectors.

Snail constructs with a lysine (K)-to-arginine (R) mutation were generated via site-directed mutagenesis to introduce a sense mutation into the *SNAI1*-coding sequence at Lys146 or Lys187. A wild-type Snail expression vector purchased from OriGene (Rockville, MD, USA) was used as the template for mutagenesis. The primer sequences were as follows: Snail K146R forward, 5′-CTCTGAGGCCAGGGATCTCCAGG-3′ and reverse, 5′-AGCTGGGCCAGCTGCTTG-3′; Snail K187R forward, 5′-AACCTGCGGGAGGGCCTTCTCTAG-3′ and reverse, 5′-CCGCAGACGCAGGGCAGC-3′. All sequences were confirmed by DNA sequencing.

2.5 | Immunoprecipitation (IP)

For IP, cell lysates were mixed with an equal amount of co-immunoprecipitation (Co-IP) buffer {40 mmol/L HEPES (pH 7.4), 120 mmol/L NaCl, 2 mmol/L ethylenediaminetetraacetic acid (EDTA), 0.3% 3-[(3-cholamidopropyl) dimethyl-ammonio]-1-propane sulfonate (10810118001, Sigma), 10 mmol/L pyrophosphate (221368, Sigma), 10 mmol/L glycerophosphate (G9422, Sigma), 50 mmol/L NaF, and a phosphatase and protease inhibitor cocktail}. Cell lysates (1 μg protein) were incubated with anti-FLAG®M2 Affinity Gel (A2220, Sigma) or anti-acetyl-lysine antibody-coated agarose (ICP0388, ImmuneChem Pharmaceuticals, Burnaby, BC, Canada) overnight with gentle rocking at 4°C. The immunoprecipitates were then washed three times in IP buffer, and the immunoprecipitated complexes were eluted by boiling for 5 min in IP buffer. After sodium dodecyl sulfate polyacrylamide gel electrophoresis, protein transfer to nitrocellulose membranes, and blocking, the membranes were incubated overnight at 4°C with primary antibodies, followed by three rounds of washing with Tween-PBS buffer and then incubation with an appropriate secondary antibody to detect intact IgG for 1 h at 25°C. The following antibodies were used at a 1:1000 dilution: mouse monoclonal anti-Snail, rabbit monoclonal anti-TFEB, rabbit polyclonal anti-acetyl-lysine, mouse

monoclonal anti-phosphoserine/threonine, rabbit monoclonal anti-HSP90, VeriBlot for IP Detection Reagent (HRP) (#ab131366, Abcam) and anti-mouse IgG for IP (HRP) (#ab131368, Abcam). Mouse monoclonal anti-β-actin was used at a 1:3000 dilution. Signals of immunoreactive bands were visualized with a Pierce ECL Western blotting substrate or SuperSignal West Pico PLUS chemiluminescent substrate. The relative abundance of individual proteins was measured by quantifying the intensities of individual protein bands on the Western blots using ImageJ software.

2.6 | Acetyl-coenzyme A (CoA) measurement

The intracellular acetyl-CoA level was calculated in the picomolar range using the PicoProbe Acetyl-CoA Assay Kit (K317, BioVision, Milpitas, CA, USA) according to the manufacturer's instructions. Briefly, cells were washed with cold PBS and sonicated in acetyl-CoA assay buffer. After centrifugation (10,000 × g, 4°C for 10 min) the supernatant was deproteinized using spin columns with a 10-kDa molecular weight cutoff. The filtrate was incubated with 10 μL of CoA quencher followed by 2 μL of quencher remover. Fifty microliters of acetyl-CoA reaction mixture containing the substrate mix, conversion enzyme, enzyme mix and picoprobe was subsequently added and incubated at 37°C for 30 min. Fluorescence was measured (Ex/Em = 535/589 nm) with an Envision Multimode Plate Reader (2105-0010, PerkinElmer, Waltham, MA, USA). After correction for the matched background well (acetyl-CoA reaction mixture added without conversion enzyme) of all readings, the values for each sample were normalized to the protein concentration in each sample determined by the Bradford protein assay.

2.7 | Citrate assay

The intracellular citrate level was calculated in the picomolar range using a citrate assay kit (K655, BioVision) following the manufacturer's instructions. After sonication of cells harvested in citrate assay buffer, the supernatant was deproteinized using spin columns with a 10-kDa molecular weight cutoff and incubated with 50 μL of citrate reaction mixture containing the enzyme mix, developer and citrate probe for 30 min at 25°C. The citrate content was measured by determining the optical density (OD) at 570 nm with an Envision Multimode Plate Reader. After correction for the matched background well (citrate reaction mixture added without enzyme mix) of all readings, the values for each sample were normalized to the protein concentra-

tion in each sample determined by the Bradford protein assay.

2.8 | In vitro invasion assay

For analysis of two-demensional (2D) invasion, inserts were precoated with 300 μg/mL Matrigel (354234, Corning, Corning, NY, USA). After trypan blue staining (1450013, Bio-Rad), 1×10^5 live cells of a series of cell lines derived from HBEC30KT cells (hb30, hb30-P, hb30-KP, and hb30-KPL cell lines) in 0.5% ACL4 medium were seeded in each 8-μm pore size cell culture insert (3422, Costar, Washington, DC, USA). Then, 10% ACL4 medium was added to the chamber below the insert. For lung and pancreatic cancer cell lines, cells were seeded in 1% RPMI-1640 medium, and 20% RPMI-1640 medium was added to the chamber below the insert. Then, the plates were incubated at 37°C for 24 h. After incubation, the inserts were fixed with 3.7% formaldehyde for 10 min at 25°C, permeabilized with 100% methanol for 10 min at 25°C, washed, and stained with 0.4% crystal violet for 30 min at 25°C. The top membrane was cleaned, washed, and dried. The number of invaded cells was quantified using ImageJ software.

A 3D spheroid cell invasion assay was performed using the Cultrex 3D Spheroid Cell Invasion Assay (3500-096-K, R&D Systems, Minneapolis, MN, USA) according to the manufacturer's instructions. Briefly, cells resuspended in 1× spheroid-forming extracellular matrix (ECM) solution were seeded at a density of 4000 live cells per well in 96-well plates and incubated at 37°C for 48 h to allow spheroid formation. After the spheroids formed, they were embedded in an invasion matrix (3500-096-03, R&D Systems) and supplemented with culture medium containing 25 μmol/L STO-609 or DMSO at 37°C. The spheroids were treated again after 3 days with 25 μmol/L STO-609 or DMSO with medium replacement. The 3D spheroid invasion assay plates were incubated for a total of 7 days at 37°C, and spheroid invasion was quantified using ImageJ software. Specifically, the lengths of three independent protrusions with the longest length from the border of the spheroid were calculated for each well and used to compare the invasiveness of the spheroids. For the *ATG5* knockdown experiment, NCI-H157 cells were seeded in 96-well plates after 24 h of transfection (*siNC* or *siATG5*) and incubated for 5 days with spheroid-forming ECM solution and invasion matrix. Invasion length was analyzed in the same way as in the STO-609 experiment.

2.9 | Scratch wound healing assay

HBEC30KT progression series (hb30, hb30-P, hb30-KP, hb30-KPL) were cultured for 24-48 h to achieve 100%

confluence. A 200-μL sterile pipette tip was used to scratch the cell monolayer. Cells were then incubated in fresh ACL4 medium. For the drug treatment group, samples were treated with the above-mentioned drugs for 24 h. The scratch gap width at 24 h was measured at three different positions and compared with the gap width at 0 h.

2.10 | Immunofluorescence

Cells were seeded on coated glass coverslips and maintained in ACL4 medium for 48 h at 37°C. For fixation, cells were washed three times with PBS, incubated for 10 min in 3.7% paraformaldehyde at 25°C, washed three more times with PBS and permeabilized for 10 min at 25°C in PBS containing 0.1% Triton X-100. After additional washing (three times) in PBS, the samples were blocked in PBS containing 0.1% Triton X-100 and 5% goat serum for 30 min at 25°C. The samples were first incubated with the indicated primary antibodies (1:150) for 1 h at 25°C and then with anti-rabbit/mouse Alexa Fluor 488/568 secondary antibodies (A-11001, 11004, 11008, 11011, Thermo Fisher Scientific) for 45 min at 25°C. Then, the samples were mounted with ProLong™ Gold Antifade Mountant with DAPI (P36931, Thermo Fisher Scientific). Images were acquired with an Axio Imager M2 microscope (Carl Zeiss, Stockholm, Sweden) equipped with a 63× oil objective and analyzed with ZEN Version 3.0 software (Zeiss, Oberkochen, Germany). For NRF2 staining, NRF2 antibody (#sc-13032, Santa Cruz, Santa Cruz, CA, USA) was used. A significant shift in NRF2 distribution between cytosol and nuclei was measured using "Cyt/Nuc" ImageJ macro [12].

2.11 | Monomeric red fluorescent protein (mRFP)-green fluorescent protein (GFP)-LC3 tandem fluorescent protein quenching assay

Autophagic flux was measured in cells transfected with the autophagy tandem sensor mRFP-GFP-LC3 [13], hb30-KPL cells (2.5×10^5) were seeded on 12-well plates with coated glass coverslips and maintained for 24 h at 37°C in ACL4 medium. The next day, the cells were transfected with 1 μg of mRFP-GFP-LC3 plasmid with 3 μL of Lipofectamine 2000. After 6–8 h of transfection, the medium was replaced with medium with or without drug compounds (NAC, STO-609, acetate and SAHA). After a total of 30 h, fluorescence images were captured using an LSM 700 confocal microscope (Carl Zeiss) and analyzed with ZEN Version 3.0 software. The autophagosomes (yellow dots) and autolysosomes (only red dots) were counted from 2-3 independent experiments.

2.12 | qRT-PCR

Total RNA was isolated from cells with the RNeasy miniprep kit (74134, Qiagen, Hilden, Germany) 72 h after siRNA transfection or 12-24 h after chemical treatment. cDNA was synthesized with the TOPscript™ cDNA Synthesis Kit (EZ0054, Enzynomics, Daejeon, Korea), and qRT-PCR for the indicated genes was performed with TOPreal™ qPCR 2X PreMIX [SYBR Green with low carboxy-X-rhodamine (ROX)] (RT501M, Enzynomics). GAPDH and beta-actin were used to normalize RNA input. qRT-PCR was performed with a StepOne Plus instrument (Applied Biosystems, Waltham, MA, USA). The fold change in expression was calculated using ΔΔCt, with the indicated reference genes (*ACTB* and *GAPDH*) as endogenous controls. Primer sequences for each gene are specified in Supplementary Table S4.

2.13 | Ultraperformance liquid chromatography/quadrupole time-of-flight mass spectrometry (LC-MS)

Transfection of *ATG5* siRNA or negative control siRNA was performed in five 100-cm^2 dishes per group using hb30-KPL cells. After 48 h of incubation at 37°C, culture medium was aspirated, and the cells were washed with 5 mL of cold PBS (Mg^{2+}/Ca^{2+}-free) on dry ice. After the aspiration of PBS, metabolites were extracted by immediately adding 1 mL of 80% methanol (−80°C) to each dish and incubating for 5 min on dry ice, and the lysate was collected with a cell scraper and transferred to an Eppendorf tube on dry ice. After the sample was vortexed for 10 min in a 4°C cold room, insoluble debris was removed via centrifugation at $13,300 \times g$ for 10 min (4°C). The supernatant was transferred to a new Eppendorf tube on dry ice, and pooled extracts were stored at −80°C before LC-MS analysis.

Ultraperformance liquid chromatography (UPLC) was performed using a Waters ACQUITY™ Ultra Performance LC system (Waters MS Technologies, Manchester, UK). Chromatographic separation was carried out on an ACQUITY UPLC BEH C18 column (100 mm × 2.1 mm, 1.7 μm) at a column temperature of 40°C. The mobile phase consisted of solvent A (0.1% formic acid in water, v/v) and solvent B (0.1% formic acid in methanol, v/v). The optimized UPLC elution conditions were as follows: 0.0–1.5 min, 1% solvent B; 1.5–6.5 min, 10%–20% solvent B; 6.5–9.0 min, 20%–70% solvent B; 9.0–12.0 min, 70%–99% solvent B; 12.0–16.0 min, 99% solvent B; 16.0–17.0 min, 99%–1% solvent B; and 17.0–20.0 min, 1% solvent B. The flow rate was set at 0.3 mL/min. The injection volume was 5 μL. The effluent was infused into a SYNAPT™

G2 quadrupole time-of-flight (Q-TOF) mass spectrometer (Waters). For the positive electrospray mode, the capillary and cone voltages were set at 3.1 kV and 40 V, respectively. For the negative electrospray mode, the capillary and cone voltages were set at -2.5 kV and 40 V, respectively. The desolvation gas flow rate was set to 800 L/h at 350°C, the cone gas flow rate was set to 50 L/h, and the source temperature was set to 120°C. Discriminating metabolites between two groups were defined as variable importance in the projection (VIP) values greater than 1, P values less than 0.05, and q values of false discovery rate (FDR) less than 0.1. Peaks were then identified using the Human Metabolome Database (HMDB, version 3.0) (https://hmdb.ca/) with 10 ppm mass tolerance.

2.14 | Animal studies

All animal procedures for this study were approved by the Institutional Animal Care and Use Committee (IACUC) of Yonsei University (Seoul, Korea). Seven- to 9-week-old BALB/c-nu Slc female mice were purchased from SLC, Inc. (Shizuoka, Japan). Mice were housed in individual-ventilation cages with a computerized environmental control system (Techniplast, Varese, Lombardia, Italy). The animal room temperature was maintained at $22 \pm 2°C$ with a relative humidity of $50 \pm 10\%$. The animals were allowed at least 1 week to adapt to their laboratory housing environment before they were used in experiments. The animal experiments included two parts.

The first was the sh*SNAI1* tail vein metastasis experiment. Mice were intravenously injected via the lateral tail vein with 3×10^6 A549-luc cells with shRNA-mediated knockdown of *SNAI1* or sh*Control* in 150 μL of PBS. After 4 weeks, the animals were anesthetized with 1%–3% isoflurane via a nose cone, and the metastatic burden was monitored by bioluminescence imaging as described previously [14]. Briefly, D-luciferin (75 mg/kg) (122799, PerkinElmer) was intraperitoneally administered, and an IVIS Imaging System (IVIS 200, PerkinElmer) was used to acquire images of mice in the prone position 15 min after injection. A region of interest was drawn around the thoracic cavity, and the total photon flux was calculated for each animal. Upon CO_2 euthanasia, the lungs were harvested at 4 weeks after tail vein injection, inflated with 10% neutral buffered formalin, dissected into five lobes, and fixed for 24–48 h. Subsequently, the lung lobes were paraffin-embedded, sectioned (5 μm), and stained with H&E. Images were analyzed using commercially available software (ImageScope; Aperio Technologies, Vista, CA, USA).

The second part involved STO-609 and BMS-303141 drug treatment in tail vein metastasis experiments. For the STO-609 efficacy experiment, mice were intravenously injected via the lateral tail vein with 4.5×10^6 A549-luc cells and orally administered 150–200 μL of vehicle control or STO-609 (100 mg/kg) via oral gavage once daily for 4 weeks beginning on the day of cell injection. For the BMS-303141 efficacy experiment, mice were intravenously injected via the lateral tail vein with 3×10^6 A549-luc cells and orally administered 150–200 μL of vehicle control or BMS-303141 (100 mg/kg) via oral gavage once daily for 3 weeks beginning on the day of cell injection. After drug treatment, metastatic burden was monitored by bioluminescence imaging as described above, and upon CO_2 euthanasia, the lungs were harvested and analyzed for metastatic nodules as described above.

2.15 | Luciferase reporter assays

An hb30-KPL cell line stably expressing a CLEAR motif-driven luciferase reporter construct was generated by transducing cells with lentiviral particles expressing Lenti-5× CLEAR Rluc-CMV-mCherry-T2A-Puro and then performing 3 μg/mL puromycin selection. A Renilla Luciferase Assay System (E2810, Promega) was used to detect luciferase activity after the designated treatments based on the protocol provided by the manufacturer. For comparison of TFEB reporter activity among cell lines (hb30, hb30-KP, and hb30-KPL), the pGL4.70 5× CLEAR Rluc and pGL4.14-firefly luciferase (Fluc) vectors (E6691, Promega) were transiently co-transfected at the same time with Lipofectamine 2000, and normalized luciferase activity (calculated by dividing the luminescent signal from the Renilla reporter gene by the firefly luminescent signal) was assessed with a Dual-Luciferase® Reporter Assay System (E1910, Promega) based on the protocol provided by the manufacturer.

2.16 | ROS assays

Intracellular ROS were detected using chloromethyl dichlorodihydrofluorescein diacetate, acetyl ester (CM-H2DCFDA) (C6827, Thermo Fisher Scientific) according to the manufacturer's instructions. Briefly, 5000 hb30-KP and hb30-KPL cells were initially seeded per well in a 96-well plate. The next day, the cells were stained with 5 μmol/L CM-H2DCFDA at 37°C for 30 min, and the medium was replaced with Earle's balanced salt solution (EBSS) (Welgene, Gyeongsan, Korea). Fluorescence was measured (Ex/Em = 485/535 nm) with a Varioskan Flash 4.00.53 Spectral Scanning Multimode Reader (Thermo Fisher Scientific). After correction for the background of all readings (subtracting the value in the background well

without DCFDA from the value in the sample well with DCFDA), the values for each sample were determined and normalized to the value of estimated live cell content using CellTiter-Glo Luminescence Cell Viability assay (G7570, Promega).

Mitochondrial ROS were detected using the MitoSOX mitochondrial superoxide indicator (M36008, Thermo Fisher Scientific) according to the manufacturer's instructions. Briefly, 3000–7000 K cells (NCI-H1155, NCI-H358, NCI-H441, HCC461) and KL cells (A549, HCC44, NCI-H157, NCI-H647) were initially seeded per well in a 96-well plate. The next day, the cells were stained with MitoSOX at 37°C for 20 min, and the medium was replaced with EBSS. Fluorescence was measured (Ex/Em = 510/580 nm) with a Varioskan Flash 4.00.53 Spectral Scanning Multimode Reader. After correction for the background of all readings (subtracting the value in the background well without MitoSOX from the value in the sample well with MitoSOX), the values for each sample were determined and normalized using CellTiter-Glo Luminescence Cell Viability assay.

2.17 | Multiplex fluorescence immunohistochemistry (IHC)

Paraffin sections of human lung adenocarcinoma (LUAD) tissues from a tumor tissue microarray (TMA) containing 92 lung cancer samples and 88 matched normal tissues (HLugA180Su03, US Biomax, Derwood, MD, USA) were were deparaffinized in Bond dewax solution (AR9222, Leica Biosystems, Baden-Wurttemberg, Germany) and rehydrated in absolute ethanol (1.07017, Merck, Burlington, MA, USA), and antigen retrieval was performed by boiling in 10 mmol/L sodium citrate (pH 6) for 20 min. Epitope retrieval was performed using BOND Epitope Retrieval Solution 2 kits (AR9640, Leica Biosystems). Immunofluorescence signals were visualized using an OPAL 7-Color Automation IHC Kit (NEL82100KT, Akoya Biosciences, Marlborough, MA, USA): tyramide signal amplification (TSA) dyes 520 (1:1200, #HPA029100, rabbit polyclonal anti-lysosomal associated membrane protein 2 (LAMP2), Atlas Antibodies, Bromma, Stockholms, Sweden, RRID: AB_10795022), 690 (1:400, rabbit polyclonal anti-acetyl-lysine), 620 (1:300, #HPA069985, rabbit polyclonal anti-Snail, Atlas Antibodies, RRID: AB_2732146) and spectral DAPI. Briefly, the slide was incubated with primary antibody for LAMP2 for 30 min, followed by detection using Polymer HRP Ms+Rb (ARH1001EA, Akoya Biosciences) for 10 min. Visualization was accomplished using Opal 520 TSA (dilution 1:150) for 10 min, and treatment with Bond Epitope Retrieval 1 (AR9961, Leica

Biosystems) for 20 min was performed. In a serial fashion, the slide was stained with two more primary antibodies for acetyl-lysine and Snail and visualized with Opal 690 TSA and Opal 620 TSA, respectively. The slide was subsequently visualized with DAPI, coverslipped using HIGHDEF® IHC fluoromount (ADI-950-260-0025, Enzo, Farmingdale, New York, USA) and scanned using a Vectra® 3.0 Automated Quantitative Pathology Imaging System (PerkinElmer). Color separation, cell segmentation, and cell phenotyping were performed with inForm Advanced Image Analysis software (version 2.2, PerkinElmer) to extract image data. For analysis, we assigned each core a representative value by multiplying the percentage and the median intensity of positively stained cells for each marker.

2.18 | IHC for metastatic tumor samples

Tumors were fixed in 10% neutral formalin for 24 h. Fixed tissues were cleared with xylene and embedded in paraffin to make slide sections (4 μm). Unstained paraffin slides were dewaxed and rehydrated. Antigen retrieval was performed with proteinase K (#S3020, DAKO, Carpinteria, CA, USA) for 10 min, and endogenous peroxidase was inactivated with 3% hydrogen peroxide (3059, Duksan, Ulsan, Korea) for 10 min. After being washed in TBS, slides were incubated for 1 h at 25°C with anti-Snail antibody (1:100, #NBP1-80022, Novus Biologicals, Littleton, CO, USA). This was followed by incubation for 20 min with anti-rabbit IgG antibody (#k4003, DAKO). The slides were subsequently washed with TBS, covered with diaminobenzidine (DAB) (#k3468, DAKO), and counterstained with hematoxylin for 10 min. After dehydration with ethanol and xylene, the slides were mounted.

2.19 | Normalization and preprocessing of public gene expression data

Gene expression data for samples in The Cancer Genome Atlas (TCGA)-LUAD cohort were directly downloaded using the TCGA biolinks R package (https://bioconductor.org/packages/release/bioc/html/TCGAbiolinks.html). Fragments per kilobase of transcript per million mapped reads (FPKM) values were transformed into log2(FPKM + 1) values and converted into z scores across samples. Gene expression microarray datasets [Gene Expression Omnibus (GEO) accession numbers GSE41271 and GSE72094] were downloaded, and values were log2 transformed.

2.20 | Public cancer cell line data

Mutation and metabolomic data of LUAD cell lines in the cancer cell line encyclopedia (CCLE) were directly downloaded from the CCLE data portal (https://portals.broadinstitute.org/ccle). Cell lines bearing any missense mutation in *KRAS* and any nonsilent mutation in *LKB1* were denoted "KL". Cell lines with a *KRAS* mutation but no *LKB1* mutation were denoted "K". Several cell lines, such as HCC2108, were assigned to either KL or K group based on protein evidence from previous researches [15, 16].

2.21 | Inference of transcription factor activity

We collected information on transcription factors for target genes from various sources: SNAI1 [17], SNAI2 [18], TWIST1 [19], ZEB1 [18], and ZEB2 [20]. Only genes exhibiting a significant correlation ($P < 0.05$, Spearman rank correlation test) with the expression level of each transcription factor in TCGA-LUAD samples were considered targets. Genes with a positive correlation were considered upregulated, and genes with a negative correlation were considered downregulated. For each sample, we conducted a modified version of gene set enrichment analysis (GSEA), single-sample GSEA (ssGSEA) [21], with target genes of transcription factors. The activity of each transcription factor was calculated by subtracting the ssGSEA score of the downregulated genes from the ssGSEA score of the upregulated genes.

2.22 | Survival analysis

We collected clinical data from TCGA-LUAD, GSE41271, and GSE72094 datasets. Based on the ssGSEA score of each sample, we classified the samples into the low and high ssGSEA score groups with varying threshold of ssGSEA score, estimated their prognoses by Kaplan-Meier survival estimators and assessed the significance of differences by log-rank tests. The survival time since initial diagnosis was used for TCGA-LUAD and GSE72094, while the survival time after surgery was used for GSE41271. The hazard ratio (HR) was calculated to define the effect on prognosis.

For TMA-based survival analysis, the total or nuclear Snail protein intensity values were obtained by multiplex fluorescence IHC. These values were used as the threshold for dividing patients into the low and high Snail protein expression subgroups. With varying threshold of Snail expression score, we estimated their prognoses by Kaplan-Meier survival estimators. Differences in the overall survival after surgery of the low and high expression groups were estimated by the log-rank test.

2.23 | Analysis of proteomic data

Protein abundance and mutation data from the clinical proteomic tumor analysis consortium (CPTAC) cohort [22] were used for the analysis. Tumors bearing *KRAS* mutations with nonsynonymous or frameshift mutations in *LKB1* and/or mono- or biallelic loss of the *LKB1* locus were denoted as KL. *KRAS*-mutated tumors other than *KRAS*-*LKB1* co-mutated tumors were denoted as K. Tumors without *KRAS* mutations were denoted as Others. Two-tailed Wilcoxon rank-sum test was used to compare two groups. Correlation *P* values were calculated by Spearman's test.

2.24 | Statistical analyses

All statistical tests were performed using the statistical software package R (ver. 4.0.0) (R foundation, Vienna, Austria). We performed two-tailed Student's *t*-tests and used the Spearman rank correlation test to assess correlations between two variables. $P < 0.05$ was considered statistically significant. R version 4.0.0 [(2020-04-24), platform: x86_64-w64-mingw32/x64 (64-bit), operating system: Windows 10 × 64 (build 18363)] was used.

3 | RESULTS

3.1 | Snail drived invasion and was associated with therapeutic resistance in KL cells

As previous studies have demonstrated that high levels of EMT-related signaling underlie the invasive and metastatic behavior of KL NSCLC [4, 23], we first examined the expression of EMT-related proteins and the behaviors of various lung cancer cell lines. Western blotting of a series of cell lines derived from normal human bronchial epithelial cells (HBEC30KT abbreviated as hb30) that model cancer progression with stepwise stable suppression of TP53 (HBEC30KT-shTP53; abbreviated as hb30-P), stable expression of KRAS G12V (HBEC30KT-shTP53/KRAS G12V; abbreviated as hb30-KP), and stable suppression of LKB1 (HBEC30KT-shTP53/KRAS G12V/shLKB1; abbreviated as hb30-KPL) (Supplementary Figure S1A) [4, 24] demonstrated that hb30-KPL cells expressed vimentin (a mesenchymal marker) but not E-cadherin (an epithelial marker) (Supplementary Figure S1B). Moreover, hb30-KPL cells showed elevated levels of the EMT-inducing

transcription factors Snail and Twist (Supplementary Figure S1B). Additionally, hb30-KPL cells showed the most prominent invasion and migration (Figure 1A, Supplementary Figure S1C). As Snail, Slug, Zeb1, and Twist are the best-known EMT transcription factors in lung cancer [25], we compared their expression levels in various *KRAS^mut/LKB1^wt* (abbreviated as "K") lung cancer cell lines (NCI-H1155, NCI-H358, NCI-H441, HCC461) and *KRAS^mut/LKB1^mut* (abbreviated as "KL") lung cancer cell lines (A549, NCI-H157, NCI-H647, HCC44, NCI-H460) by Western blotting. Among these transcription factors, Snail expression showed the strongest elevation in the KL and hb30-KPL cell lines as compared to the K and hb30-KP cell lines, respectively (Figure 1B, Supplementary Figure S1B). Increased Snail activity was also observed in LUAD tumor tissues from both the TCGA cohort and the CPTAC cohort: decreased *CDH1* (E-cadherin), the most well-known transcriptional repression target of Snail [26], in KL tumors in TCGA data and a positive correlation between LKB1 and E-cadherin protein levels in CPTAC data (Supplementary Figure S1D). In addition, the degree of invasiveness significantly differed between K and KL cell lines (Figure 1C), suggesting that there may be a positive trend between Snail levels and invasiveness.

Consistent with this finding, the high *SNAI1* target gene expression was strongly associated with short overall survival in three independent LUAD patient cohorts (TCGA, GSE72094, and GSE41271) (Figure 1D), while other transcription factors showed inconsistent or even opposite results (Supplementary Figure S1E). Based on these data, KL lung cancer cell lines expressed high levels of Snail, which was associated with aggressive behavior in vitro and poor patient survival.

We next examined how *KRAS-LKB1* co-mutation affected Snail expression and thus the behavior of KL cancer cells. We knocked down the expression of *KRAS* or ectopically expressed *LKB1* and examined the protein levels of Snail. Both *KRAS* knockdown and ectopic expression of *LKB1* led to reductions in Snail protein expression (Supplementary Figure S1F). Moreover, compared with knockdown of other EMT factors, *SNAI1* knockdown most significantly suppressed the invasion of KL cell lines (Figure 1E). A tail vein injection model of experimental metastasis demonstrated that the BALB/c-nude mice injected with *SNAI1*-knockdown KL A549 cells showed significantly less metastasis than the control mice injected with empty vector-harboring A549 cells (Figure 1F and G). These data suggest that a KL-driven increase in Snail is required for the metastasis of KL cells.

Accumulating evidence suggests that co-mutation of *LKB1* in *KRAS*-mutated cancers confers therapeutic resistance [8, 27, 28]. Considering these results and the finding that EMT-activated *KRAS*-mutated cancers were resistant

to the depletion of oncogenic *KRAS* [5], we evaluated the sensitivity of three KL NSCLC cell lines (HCC44, H2122 and H2030), carrying the *KRAS* (G12C) mutation and with elevated Snail expression (Figure 1B, Supplementary Figure S1G), to a KRAS (G12C) inhibitor AMG-510 [29]. We observed complete resistance of H2122 cells to all tested concentrations (0.01–10 μmol/L) and cytostatic or minor cytotoxic effects on HCC44 cells (Supplementary Figure S1H). Intriguingly, in addition to exhibiting reduced efficacy in KL cell lines, AMG-510 treatment showed enhanced invasion of HCC44 and H2122 cells accompanied with elevated Snail expression (Supplementary Figure S1I-S1J). These data suggest that KRAS G12C inhibitors may have limited therapeutic value and may even facilitate metastasis in at least some KL tumors.

Overall, these results indicate that in KL cancer cells, elevated Snail expression drives invasion and may be related to therapeutic resistance.

3.2 | LKB1 loss impaired antioxidant defenses, resulting in increased ROS levels and Snail stabilization in KL cells

To identify effective treatment strategies for the KL patient subgroup, we aimed to further elucidate the molecular mechanisms driving Snail accumulation. As *LKB1* loss has been shown to cause ROS accumulation [30–32], we examined the ROS levels in K and KL lung cancer cell lines by performing CM-H2DCFDA and MitoSOX assays. Indeed, the hb30-KPL and KL cell lines exhibited higher ROS levels than the hb30-KP and K cell lines, respectively (Figure 2A and B). Moreover, the expression of most of the assayed antioxidant genes was significantly lower in the hb30-KPL and KL cell lines than in the hb30-KP and K cell lines, respectively (Supplementary Figure S2A-S2B), suggesting that the increased ROS levels in these cell lines resulted from the decreased expression of antioxidant genes. Thus, the addition of an *LKB1* mutation in a *KRAS*-mutated background appears to result in an increase in ROS levels due to reduced expression of antioxidant genes.

NF-E2-related factor 2 (NRF2) is the master regulator of antioxidant responses [33], competing with p62 to bind Keap1 under oxidative stress conditions, thereby being protected from the Keap1-mediated proteasomal degradation [33–35]. In hb30-KPL cells, *LKB1* loss caused defects in the induction of p62 and the antioxidant enzyme *HMOX-1* in response to increased ROS stress (Figure 2C). Even under steady-state growth conditions, hb30-KPL cells had lower phospho-p62 (Ser351) protein levels and nuclear NRF2 protein levels than hb30-KP cells (Figure 2D), suggesting that p62 downregulation impairs NRF2 stability in hb30-KPL cells. This trend was also observed in LUAD
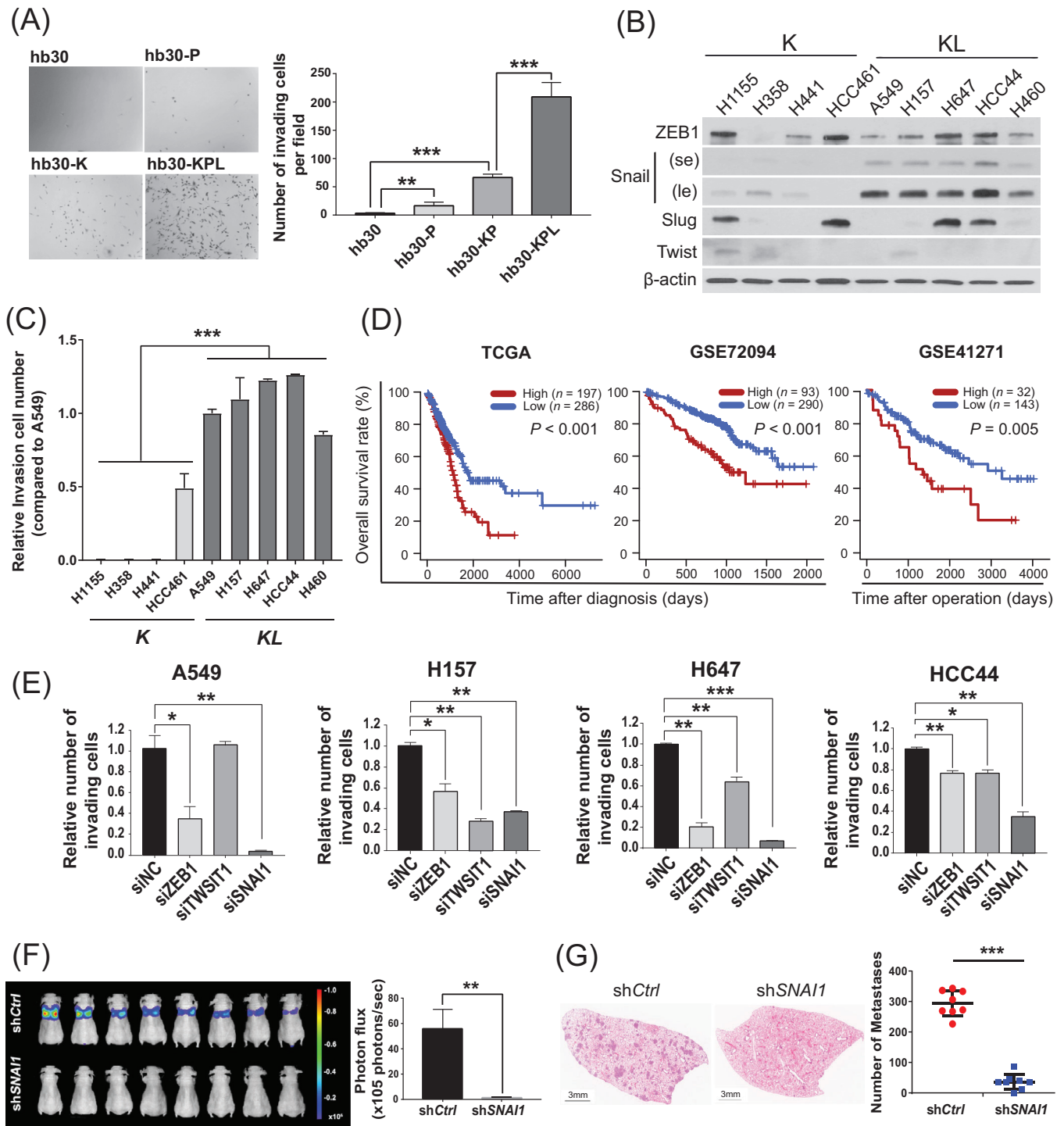
FIGURE 1 Snail drives invasion and is associated with therapeutic resistance in KL lung cancer cells. (A) Matrigel invasion assay of HBEC30KT-derived cell lines (HBEC30KT abbreviated as hb30, HBEC30KT-shTP53 abbreviated as hb30-P, HBEC30KT-shTP53/KRAS G12V abbreviated as hb30-KP, HBEC30KT-shTP53/KRAS G12V/shLKB1 abbreviated as hb30-KPL) in the progression series. Representative bright-field micrographs (20×) of cells that invaded through Matrigel-coated Transwell membranes are shown in the left panel, and quantification data of invaded cell numbers are shown in the right panel. (B) Steady-state accumulation of the indicated proteins was assessed by Western blotting of whole-cell lysates from the indicated *KRAS*-mutated (K) and *KRAS-LKB1* co-mutated (KL) lung cancer cell lines. Beta-actin was used as the loading control. se, short exposure; le, long exposure. (C) Matrigel invasion assay of K and KL cell lines. (D) Kaplan-Meier estimates of overall survival with three independent LUAD cohorts (TCGA, GSE41271, and GSE72094) divided by low and high ssGSEA scores of the *SNAI1* target genes indicated by arrowheads in Supplementary Figure S1E. Comparison of survival was based on the log-rank test. (E) Matrigel invasion assay of four KL cell lines (A549, NCI-H157, NCI-H647, and HCC44) treated with the indicated siRNAs. Relative invaded cell numbers are expressed as the fold change relative to the *siNC*-treated cells. (F) Effect of *SNAI1* knockdown on

tissues from the CPTAC cohort, wherein decreased p62 and glutathione peroxidase 1 (GPx1) (NRF2 target) levels were observed in KL tumors and these two proteins were positively correlated with LKB1 protein levels (Supplementary Figure S2C). Collectively, these data indicate that ROS are maintained at high steady-state levels in hb30-KPL cells due to the suppression of p62, which impairs the NRF2-dependent antioxidant response.

Elevated oxidative stress activates AMPK to limit mitochondrial ROS production through various mechanisms [36]. We therefore examined whether the increased levels of ROS in KL lung cancer cells might activate AMPK by promoting phosphorylation of Thr172 within the activation loop [37]. Indeed, we observed higher phospho-AMPK T172 levels in hb30-KPL cells than in hb30-KP cells (Figure 2E). Furthermore, we observed that *AMPK* knockdown in hb30-KPL cells reduced invasion (Figure 2F), indicating that ROS-driven AMPK activation enhances invasion in hb30-KPL cells.

Next, we investigated whether modulating steady-state ROS levels in hb30-KPL cells affects AMPK activation. AMPK phosphorylation at T172 was increased by H_2O_2 treatment, whereas it was decreased by NAC treatment (Figure 2G). Moreover, concordant changes in the Snail level were observed in response to the same perturbations (Figure 2H). We further confirmed that the KEAP1 antagonist CDDO-ME stabilized NRF2, thereby decreasing phospho-AMPK T172 and Snail (Figure 2I), and that p62 overexpression destabilized Snail (Figure 2J). Thus, ROS was sufficient to drive AMPK activation and the consequent increase in Snail in hb30-KPL cells.

AMPK activation during cellular energy stress is mediated by LKB1 [38]. It has also been shown that ROS-driven AMPK activation occurs through CAMKK2 activation via increased intracellular calcium levels [39]. Therefore, we hypothesized that activated CAMKK2 may be responsible for the activation of AMPK and the increase in downstream Snail in KL cells and examined this process by Western blotting. Indeed, hb30-KPL cells showed a higher level of phospho-CAMKII T286, a biomarker correlated with intracellular calcium levels [40], than hb30-KP cells (Figure 2K). The inhibition of calcium signaling in hb30-KPL cells by either BAPTA-AM, a calcium chelator, or calmidazolium chloride, a calmodulin inhibitor, decreased AMPK phosphorylation as well as the Snail levels (Supplementary Figure S2D), further supporting this hypothesis. We also observed that both *CAMKK2* knockdown and chemical CAMKK2 inhibition with the inhibitor STO-609 reduced the phospho-AMPK T172 and Snail levels in hb30-KPL and KL cell lines, similar to the effects of ROS or calcium signaling inhibition (Figure 2L and M, and Supplementary Figure S2E-S2F). Intriguingly, STO-609 effectively suppressed the aberrant activation of AMPK and the increase in Snail by exposure to AMG-510 in KL cancer cell lines (Supplementary Figure S2G). Finally, CAMKK2 inhibition reduced the 2D and 3D invasion and migration of hb30-KPL and H157 (KL) cells (Figure 2N and O, Supplementary Figure S2H-S2I). Taken together, these results indicate that ROS elevation due to the impaired antioxidant defense capacity in KL lung cancer cells causes the activation of the ROS/Ca^{2+}-CAMKK2-AMPK pathway, which leads to elevated Snail levels and an invasive phenotype.

3.3 | CAMKK2-AMPK-dependent activation of autolysosomes drived invasion through GSK3β-independent Snail stabilization

AMPK functions in various aspects to maintain energy balance during metabolic stress [37], including activation of autophagy through phosphorylation of ULK1 [41]. We previously reported that lysosomal activity was specifically increased in KL cells [4], and thus, we hypothesized that Snail stabilization by AMPK activation may occur through the autophagy-lysosomal pathway. To assess the role of the ROS-CAMKK2-AMPK pathway in driving autophagy in KL cells, we investigated whether perturbations of the pathway affect microtubule-associated protein 1A/1B-LC3 turnover and delivery of mRFP-GFP-LC3 to lysosomes. In hb30-KPL cells, 81% of LysoTracker-positive vesicles colocalized with LC3 (Figure 3A), indicating that the majority of these vesicles were autolysosomes. Indeed, inhibiting lysosomal function with CQ resulted in increased levels of LC3-II, and the CQ+/CQ− LC3-II

---

tumor metastasis in the A549-luc tail vein injection model. A549-luc cells with or without *SNAI1* knockdown were injected into nude mice via the tail vein (8 mice per group). Bioluminescence images of the mice in each group at 4 weeks post-injection are shown (left). The total metastatic burden was estimated by measuring the photon flux (right). The data are presented as the mean ± SEM. (G) Representative images of H&E staining of lung sections from the control group and *SNAI1*-knockdown group (left). Number of metastatic nodules in the lung for each group (right). All experiments were performed in triplicate unless otherwise indicated. The data are presented as mean ± SD, unless otherwise indicated. Significant differences between groups were determined by a two-sided unpaired Student's *t*-test. *$P < 0.05$, **$P < 0.01$, ***$P < 0.001$. Abbreviations: LKB1, liver kinase B1; ZEB1, zinc finger E-box binding homeobox 1; LUAD, lung adenocarcinoma; TCGA, The Cancer Genome Atlas; ssGSEA, single sample Gene Set Enrichment analysis; NC, negative control; SEM, standard error of the mean; H&E, hematoxylin and eosin
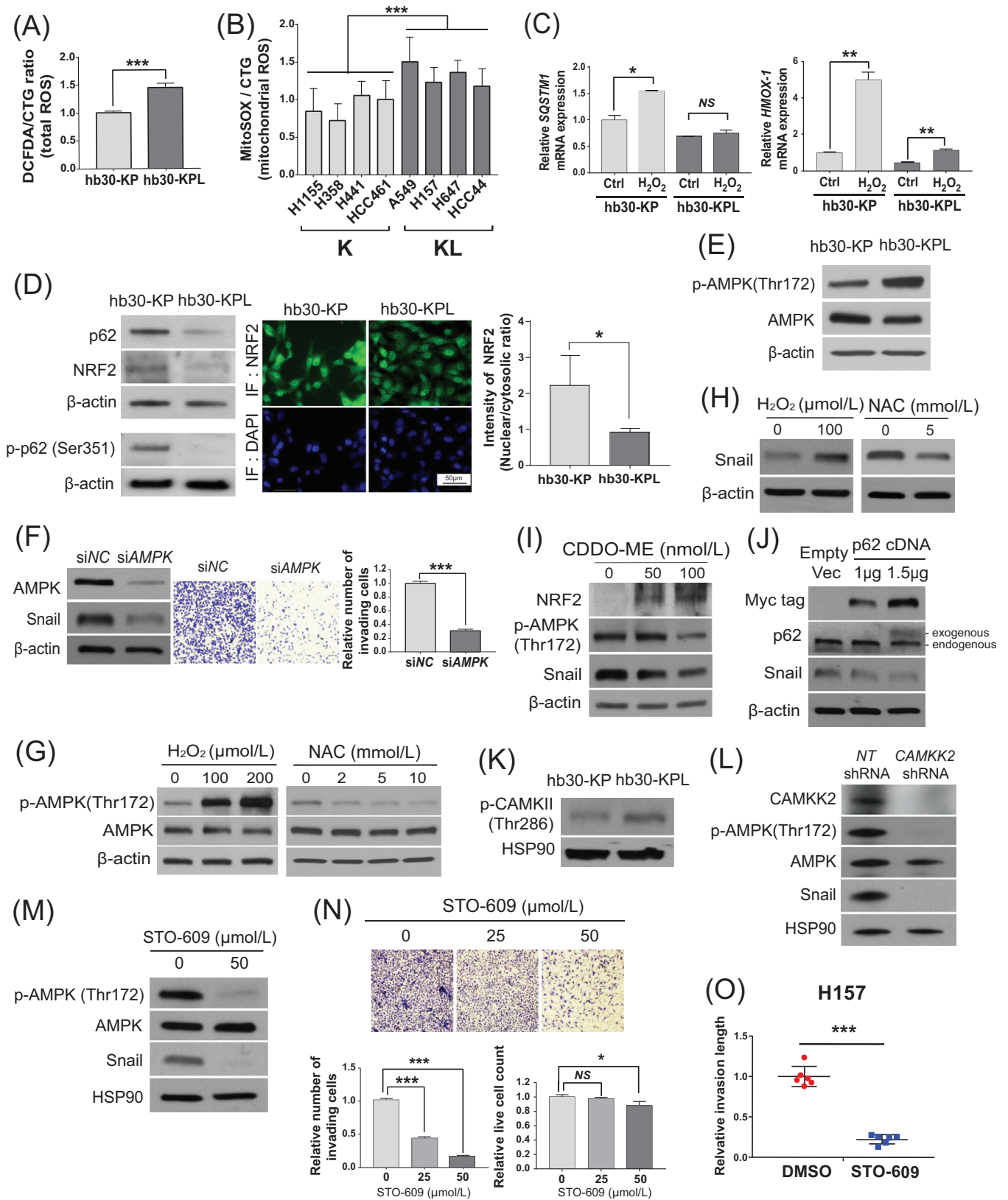
FIGURE 2 *LKB1* loss impairs antioxidant defenses, resulting in increased reactive oxygen species (ROS) levels and Snail stabilization in KL cells. (A) ROS levels detected using the CM-H2DCFDA probe in hb30-KP and hb30-KPL cells. (B) Mitochondrial ROS levels in four K and four KL cell lines. The bar plots show the mean ± SD of four independent experiments. (C) Real-time PCR analyses of the relative expression of the indicated genes in hb30-KP and hb30-KPL cells exposed to 150 μmol/L H_2O_2 for 6 h (2 RNA samples from each cell line). All data are presented as the fold change ± SD compared to control cells without H_2O_2 exposure. (D) Steady-state accumulation of the p62, phospho-p62

ratio indicated that hb30-KPL cells had higher basal autophagic flux than hb30-KP cells (Figure 3B). This elevated autophagic flux in hb30-KPL cells was decreased by treatment with NAC or STO-609, as evidenced by the decreased CQ+/CQ− LC3-II ratios in the LC3 turnover assay (Supplementary Figure S3A) and the decreased autophagosome (mRFP+/GFP+) and autolysosome (mRFP+/GFP−) numbers in the mRFP-GFP-LC3 lysosome delivery assay (Supplementary Figure S3B). Thus, increased autophagic flux in hb30-KPL cells is driven by ROS/CAMKK2 signaling.

The CLEAR network regulates lysosomal biogenesis and participates in macromolecule clearance via lysosome-associated processes, including autophagy [42]. TFEB directly binds to specific E-box sites at CLEAR gene network promoters [43] and transactivates CLEAR network genes [44]. Thus, we speculated that activated autophagy in the KL context might be at least partly due to CLEAR activation via TFEB. To test this hypothesis, we evaluated TFEB activity by transfection of a CLEAR motif-driven luciferase reporter construct. We confirmed that the activated autophagic flux in hb30-KPL cells was at least partially due to increased CLEAR activity based on TFEB activity (Figure 3C). We found that *AMPK* or *KRAS* knockdown and ectopic expression of *LKB1* resulted in a reduction in TFEB levels (Supplementary Figures S1F and S3C). As measured by TFEB activity, inhibition of either ROS or CAMKK2 decreased CLEAR activity (Figure 3D and E). Collectively, these data indicate that the activation of the ROS/Ca^{2+}-CAMKK2-AMPK signaling pathway induces autophagy at least partially through the TFEB-mediated activation of the CLEAR network.

Next, we sought to examine whether the activated autophagy-lysosomal system in KL cells increases Snail protein expression. We found that knockdown of crucial autophagic mediators (*ULK1, ATG5* or *TFEB*) or autophagic inhibition by CQ decreased the Snail protein levels (Figure 3F and G) but not mRNA levels (Supplementary Figure S3D), indicating that autophagy stabilizes the Snail protein. Co-treatment with the proteasome inhibitor bortezomib rescued CQ- and STO-609-induced Snail depletion (Figure 3H and I). Accordingly, we observed that Snail ubiquitination increased upon autophagic inhibition (Supplementary Figure S3E), indicating that the Snail protein is stabilized by autophagy. The ubiquitin-mediated proteasomal degradation of Snail was regulated by Snail phosphorylation, which is in turn mediated by GSK3β [45, 46]. Given the above results, we sought to determine whether Snail protein stability regulated by autolysosomal activity is dependent on GSK3β activity. Since GSK3β was fully activated through phosphorylation of Y216 [46], we first examined whether the total protein level or phosphorylation of GSK3β is regulated by autolysosomes. The levels of neither total GSK3β nor active GSK3β

(Ser351) and NRF2 proteins was assessed by Western blotting analysis of whole-cell lysates from hb30-KP and hb30-KPL cells. Beta-actin was used as the loading control (left). Detection of steady-state NRF2 protein in hb30-KP and hb30-KPL cells by immunofluorescence (scale bar, 50 μm) (middle). Analyses were performed with anti-NRF2 antibody (green). DAPI was used to visualize nuclei. The bar plots show the nuclear to cytosolic ratio of NRF2 protein intensity, quantified by ImageJ software (three independent experiments). (E) Steady-state accumulation of the phospho-AMPK protein was assessed by Western blotting analysis of whole-cell lysates from hb30-KP and hb30-KPL cells. HSP90 was used as the loading control. (F) The effects of *AMPK* knockdown in hb30-KPL cells on the accumulation of Snail and 2D invasion were evaluated by Western blotting (left) and Matrigel invasion assays (right), respectively. (G and H) Proteins from hb30-KPL cells that were untreated or treated with H$_2$O$_2$ or NAC for 6 h were analyzed by Western blotting for phospho-AMPK, total AMPK (G), and Snail (H). Beta-actin was used as the loading control. (I) Effects of treatment with the NRF2 activator CDDO-ME for 24 h on the expression of the indicated proteins in hb30-KPL cells, as determined by Western blotting. Beta-actin was used as the loading control. (J) The effects of ectopic *p62* expression on the Snail protein levels in hb30-KPL cells were determined by Western blotting 24 h post-transfection. Beta-actin was used as the loading control. (K) Steady-state accumulation of phospho-CAMKII protein was assessed by Western blotting analysis of whole-cell lysates from hb30-KP and hb30-KPL cells. HSP90 was used as the loading control. (L) Effects of *CAMKK2* knockdown by shRNA on the expression of the indicated proteins in hb30-KPL cells, as determined by Western blotting. HSP90 was used as the loading control. (M and N) The effects of treatment with the CAMKK2 inhibitor STO-609 for 24 h on Snail accumulation and 2D invasion in hb30-KPL cells were evaluated by Western blotting (M) and Matrigel invasion assays (N). Beta-actin was used as the loading control. (N) The bar plots on the bottom left show the mean relative invaded cell number ± SD, while bar plots on the bottom right show the mean relative live cell count ± SD of three independent experiments. (O) Effects of STO-609 (25 μmol/L) for 7 days on the invasion of spheroids generated from the indicated KL cell line under 3D culture conditions. The bars indicate the mean ± SD of six invasion lengths in two spheroids per group. DMSO was used as a vehicle control. All experiments were performed in triplicate unless otherwise indicated. The data are presented as mean ± SD, unless otherwise indicated. Significant differences between groups were determined by a two-sided unpaired Student's *t*-test. *$P < 0.05$, **$P < 0.01$, ***$P < 0.001$, *NS*: not significant. Abbreviations: ROS, reactive oxygen species; CM-H2DCFDA, chloromethyl dichlorodihydrofluorescein diacetate, acetyl ester; PCR, polymerase chain reaction; CTG, CellTiter Glo; NRF2, NF-E2-related factor 2; DAPI, 4′,6-diamidino-2-phenylindole; NAC, N-acetyl cysteine; AMPK, AMP-activated protein kinase, CDDO-ME, bardoxolone methyl; CAMKII, Calcium/Calmodulin-dependent Protein Kinase II; CAMKK2, calcium/calmodulin-dependent protein kinase kinase 2; 2D, two-dimensional; 3D, three-dimensional; HSP90, heat shock protein 90; DMSO, dimethyl sulfoxide
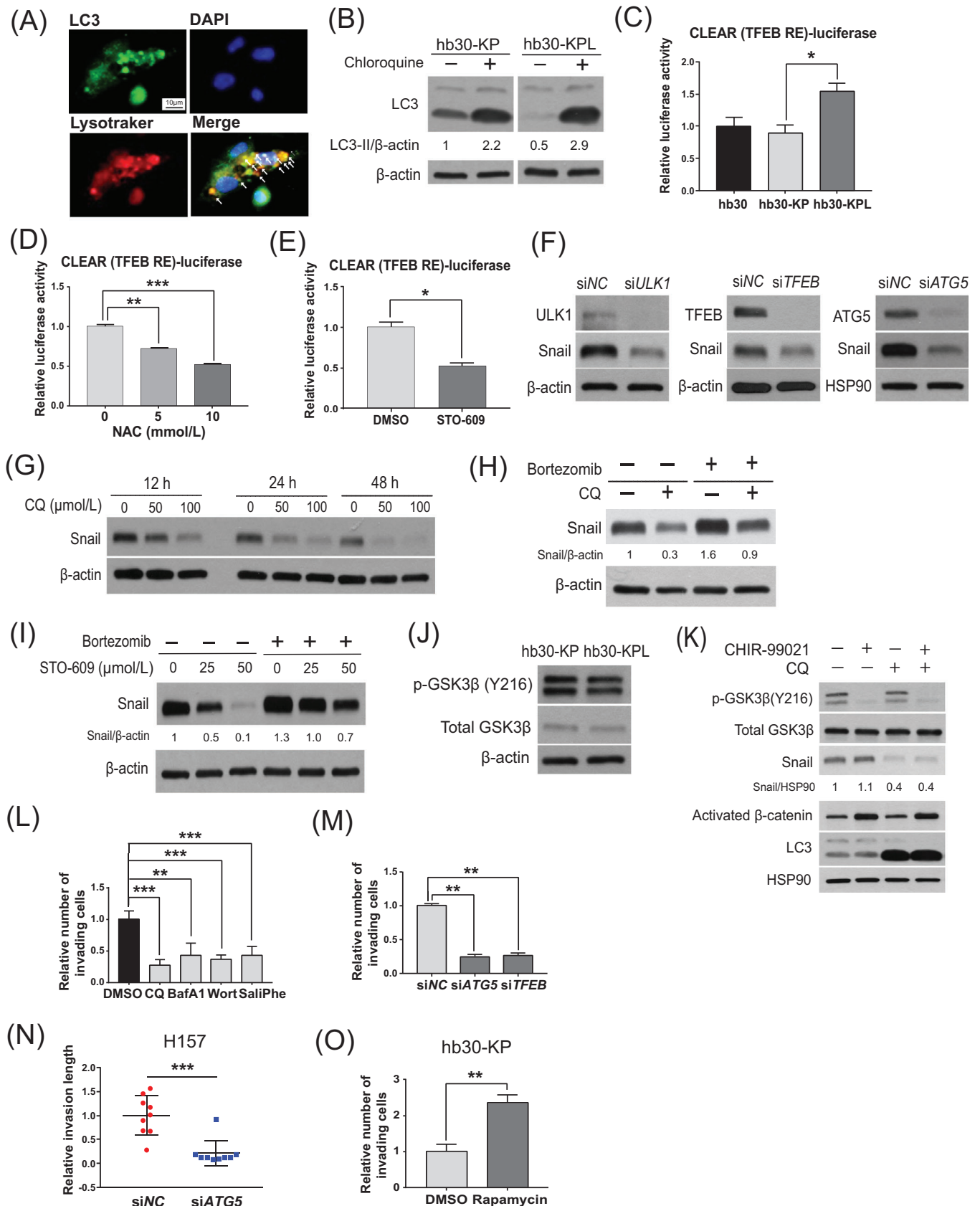
FIGURE 3 CAMKK2-AMPK-dependent activation of autolysosomes drives invasion through GSK3β-independent Snail stabilization. (A) Detection of steady-state lysosomes and autophagosomes in hb30-KPL cells by immunofluorescence (scale bar, 50 μm). LC3 (green dots) represents autophagosomes, and LysoTracker (red dots) represents lysosomes. DAPI was used to visualize nuclei. Arrows indicate cells with

(phospho-GSK3β Y216) were increased in hb30-KPL cells compared to hb30-KP cells (Figure 3J), indicating that the *KRAS-LKB1* co-mutation does not affect GSK3β activity. In addition, the phospho-GSK3β Y216 level did not increase upon autophagic inhibition (Supplementary Figure S3F), indicating that autophagy does not affect GSK3β in KL cells. Moreover, the GSK3β inhibitor CHIR-99021 did not rescue the Snail protein level when autophagy was inhibited by CQ treatment but rescued the level of activated β-catenin, another GSK3β substrate used as a control to show inhibitory activity of CHIR-99021 (Figure 3K). These results indicate that the regulation of Snail protein stability via autolysosomal activity is not dependent on GSK3β activity.

Based on the relationship between autophagy and Snail, we next investigated whether autophagy plays a pro-tumorigenic role in KL cells by promoting invasion. To examine this, we dissected the causality between autophagy and invasion using various genetic and chemical perturbations. Autophagic inhibition by various drugs or knockdown of autophagy genes (*ATG5* and *TFEB*) decreased the invasiveness and migration of hb30-KPL and KL cancer cell lines (Figure 3L–N, Supplementary Figure S3G-S3I). However, autophagic activation with rapamycin (an mTOR inhibitor) resulted in increased invasiveness of hb30-KP cells (Figure 3O), indicating that autophagy is necessary and sufficient to drive the invasive phenotype. Taken together, these data demon-strate that the CAMKK2-AMPK-dependent activation of autolysosomes drives the invasiveness of KL cancer cells by stabilizing Snail.

3.4 | Acetyl-CoA supplied by autophagy underlied the enhanced invasion of KL cells

We next examined how autophagy may drive the enhanced invasion of KL cells by examining differences in metabolite levels in K and KL cells. By analyzing a CCLE metabolomic dataset [47], we found that 14 KL cancer cell lines had higher levels of 11 of the 225 detected metabolites than 31 K cancer cell lines (Figure 4A). LC-MS revealed that among these metabolites, the levels of glutathione, gamma-aminobutyric acid (GABA), citrate, and dimethyl-glycine were significantly decreased in hb30-KPL cells upon autophagic inhibition by *ATG5* knockdown (Supplementary Figure S4A), suggesting that these metabolites are supplied by enhanced autophagy in KL cells.

Citrate is a precursor of acetyl-CoA, and accumulating evidence indicates that acetyl-CoA mediates invasion and metastasis in prostate cancer [48], breast cancer [49], and hepatocellular carcinoma [50]. Thus, we hypothesized that citrate supplied by autophagy may increase the intracellular acetyl-CoA level to support KL cell invasion. To test this hypothesis, we compared the citrate

---

co-localized LC3 and LysoTracker puncta. (B) Western blotting of LC3 proteins in hb30-KP and hb30-KPL cells in response to treatment with 50 μmol/L CQ for 6 h. Beta-actin was used as the loading control. Values obtained from a quantitative densitometric analysis of LC3-II relative to beta-actin are shown underneath the LC3 blots. (C) Steady-state relative luciferase activity in hb30, hb30-KP and hb30-KPL cells transiently transfected with a CLEAR motif-driven luciferase reporter construct. Relative luciferase intensities are expressed as the fold change relative to the hb30 control cells. (D-E) Effects of treatment with NAC (D) or 50 μmol/L STO-609 (E) for 24 h on the relative luciferase activity in hb30-KPL cells stably transfected with a TFEB-luciferase reporter construct. (F-G) The effects of genetic suppression of autophagy with the indicated siRNAs (F) or inhibition by the indicated concentrations of CQ for 12-48 h (G) on Snail protein accumulation were determined by Western blotting analysis of whole-cell lysates from hb30-KPL cells. Beta-actin and HSP90 were used as the loading control. (H and I) Effects of treatment with CQ (50 μmol/L for H) or STO-609 at the indicated concentrations for 12 h in the presence or absence of 20 nmol/L bortezomib for the last 4 h on Snail protein accumulation in hb30-KPL cells. Beta-actin was used as the loading control. Values obtained from a quantitative densitometric analysis of Snail relative to beta-actin are shown underneath the Snail blots. (J) Steady-state accumulation of the indicated proteins was assessed by Western blotting of whole-cell lysates from hb30-KP and hb30-KPL cells (left). Beta-actin was used as the loading control. (K) Effect of treatment with the GSK3β inhibitor CHIR-99021 (3 μmol/L for 5 h) in the presence or absence of 50 μmol/L CQ on Snail protein accumulation in hb30-KPL cells. HSP90 was used as the loading control. Activated beta-catenin was used as the positive control GSK3β substrate. (L,M,O) Effects of the indicated drugs: CQ (lysomotropic weak base) 25 μmol/L, bafilomycin A1 (BafA1: V-ATPase inhibitor) 10 nmol/L, wortmannin (Wort: PI3K inhibitor) 1 μmol/L, saliphenylhalamide (Sali: V-ATPase inhibitor) 10 nmol/L and rapamycin (mTORC1 inhibitor) 2 μmol/L for 24 h (L, O) or knockdown with the indicated siRNAs (M) on Matrigel invasion of hb30-KPL cells (L-M) or hb30-KP cells (O). Quantified data of cells that invaded through Matrigel-coated Transwell membranes are shown. (N) Effects of *ATG5* knockdown on the invasion of spheroids generated from the indicated KL cell line under 3D culture conditions. The bars indicate the mean $\pm$ SD of nine invasion lengths in three spheroids per group. All experiments were performed in duplicate unless otherwise indicated. The data are presented as mean $\pm$ SD, unless otherwise indicated. Significant differences between groups were determined by a two-sided unpaired Student's *t*-test. *$P < 0.05$, **$P < 0.01$, ***$P < 0.001$. Abbreviations: LC3, microtubule-associated protein 1A/1B light chain 3; DAPI, 4′,6-diamidino-2-phenylindole; CQ, chloroquine; CLEAR, coordinated lysosomal expression and regulation; NAC, N-acetyl-l-cysteine; NC, negative control; TFEB, transcription factor EB; TFEB RE, TFEB reporter; ULK1, Unc-51-like kinase; ATG5, autophagy related 5; GSK3β, glycogen synthase kinase 3 beta; HSP90, heat shock protein 90, 3D, three-dimensional; DMSO, dimethyl sulfoxide
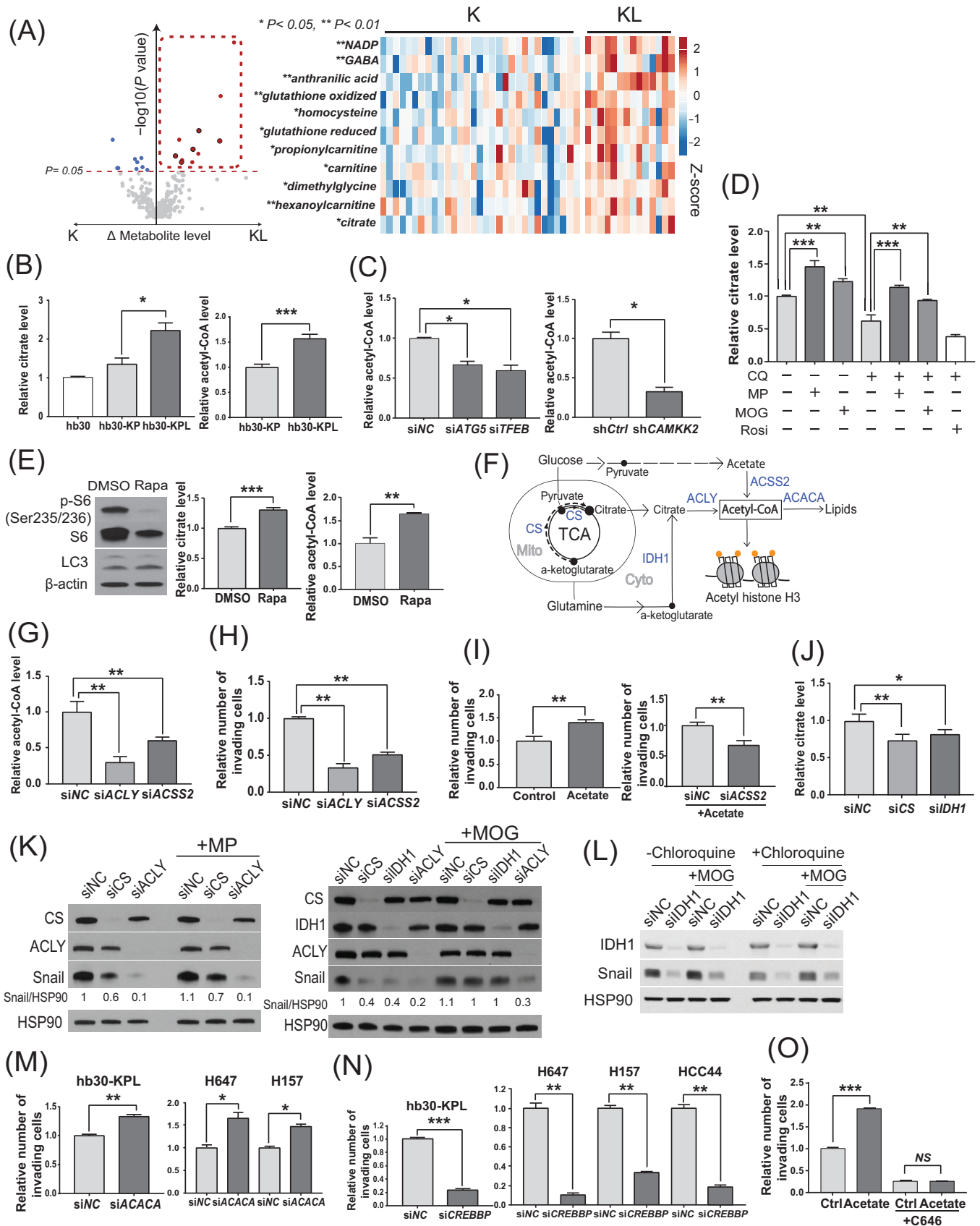
FIGURE 4 Acetyl-CoA supplied by autophagy underlies the enhanced invasion of KL cells. (A) Volcano plot of 225 metabolites compared between 14 KL and 31 K lung cancer cell lines under steady-state growth conditions based on the CCLE metabolomic data (left). Metabolites with statistically significant differences between the two sets of cells (*P* < 0.05, two-sided Wilcoxon rank sum test) are shown as

and acetyl-CoA levels in hb30-KP and hb30-KPL cells and examined whether modulation of autophagic activity affects intracellular citrate and acetyl-CoA levels. In support of this hypothesis, we found that hb30-KPL cells had higher citrate and acetyl-CoA levels than hb30-KP cells (Figure 4B). We also confirmed that the inhibition of autophagy (by siRNA or CQ) or CAMKK2 (by shRNA or STO-609) decreased citrate and acetyl-CoA levels in the hb30-KPL and KL cell lines (Figure 4C, Supplementary Figure S4B-S4D).

Intracellular citrate is synthesized mainly from two major carbon sources, pyruvate and α-ketoglutarate [51]. To further confirm that autophagy supplies citrate to generate acetyl-CoA and stabilize Snail in KL cells, we examined whether supplementation with citrate precursors could rescue the citrate and Snail levels upon autophagic inhibition. We found that the delivery of their cell-permeable forms [methyl pyruvate (MP) and dimethyl-2-oxoglutarate (MOG), respectively] almost com-

pletely reversed the effects of CQ on the citrate levels, while rosiglitazone, an inducer of mitochondrial biogenesis, did not have this effect (Figure 4D). Consistent with this result, autophagic activation by rapamycin in hb30-KP cells increased the citrate and acetyl-CoA levels (Figure 4E). Collectively, our data indicate that KL cells maintain increased levels of acetyl-CoA through citrate supplied by enhanced autophagy.

Metabolic pathways for the synthesis and degradation of citrate and acetyl-CoA are summarized in Figure 4F. To validate the causal link between citrate/acetyl-CoA and KL cell invasiveness, we evaluated KL cell invasiveness after siRNA-mediated knockdown of the expression of enzymes in these pathways. Either *ACLY* or acetyl-CoA synthetase short chain family member 2 (*ACSS2*) knockdown reduced acetyl-CoA levels (Figure 4G) and hb30-KPL and KL cell invasion (Figure 4H and Supplementary Figure S4E). Acetate treatment enhanced hb30-KPL cell invasion, which was reversed by *ACSS2*

---

colored dots. The red dots in the box enclosed by dashed lines represent statistically significantly upregulated metabolites in KL cells (delta>0), whereas the blue dots represent downregulated metabolites (delta<0) with a P value < 0.05. Delta values were obtained by subtracting the mean levels of a metabolite in K cell lines from the mean levels in KL cell lines. The black highlighting indicates metabolites downregulated upon *ATG5* knockdown in hb30-KPL cells, as shown in Supplementary Figure S4A. The heatmap depicts the cell line-specific levels of 11 metabolites significantly upregulated in KL cells (right) (B) Steady-state levels of citrate in hb30 cells, hb30-KP cells, and hb30-KPL cells. Relative absorbance is expressed as the fold change relative to the hb30 control cells (left). Steady-state acetyl-CoA levels in hb30-KP and hb30-KPL cells. Relative absorbance is expressed as the fold change relative to the hb30-KP (right). The data are shown as the mean ± SD of two and four independent experiments, respectively. (C) Acetyl-CoA level in hb30-KPL cells with the indicated genetic knockdown as a fold change relative to the control cells. (D) Levels of citrate in hb30-KPL cells treated with 8 mmol/L MP, 3 mmol/L MOG or 200 μmol/L rosiglitazone for 24 h in the presence or absence of 50 μmol/L CQ. (E) Western blotting of the indicated proteins in hb30-KP cells treated with 2 μmol/L rapamycin for 5 h. Beta-actin was used as the loading control (left). Increased conversion of LC3-I (upper band) to LC3-II (lower band) indicates autophagic activation. The levels of citrate and acetyl-CoA under the same conditions (right). (F) Schematic of acetyl-CoA metabolism in mammalian cells. Citrate is synthesized by two independent pathways via mitochondrial citrate synthase (CS) and cytosolic isocitrate dehydrogenase 1 (IDH1). Acetyl-CoA is synthesized from citrate by ATP citrate lyase (ACLY) or from acetate by acetyl-CoA synthetase 2 (ACSS2). Acetyl-CoA is then used as a precursor for synthesizing lipid molecule synthesis or as an acetyl group donor for protein acetylation. Blue text indicates enzymes. (G-H) Effects of *ACLY* or *ACSS2* knockdown on the acetyl-CoA level (measured by fluorescence intensity) (G) and Matrigel invasion (H) in hb30-KPL cells. (I) Effect of 10 mmol/L acetate treatment for 24 h on the Matrigel invasion of hb30-KPL cells (left). Matrigel invasion of hb30-KPL cells with or without *ACSS2* knockdown and 10 mmol/L acetate treatment for the last 24 h (right). (J) Effects of *CS* or *IDH1* knockdown on citrate in hb30-KPL cells. (K) Effects of *CS* or *ACLY* knockdown in the presence or absence of 8 mmol/L MP (left) or *CS*, *IDH1*, or *ACLY* knockdown in the presence or absence of 3 mmol/L MOG (right) on Snail accumulation in hb30-KPL cells, as determined by Western blotting. HSP90 was used as the loading control in both blots. Values obtained from a quantitative densitometric analysis of Snail relative to HSP90 are shown underneath the Snail blots. (L) Effect of *IDH1* knockdown and treatment with 50 μmol/L CQ in the presence or absence of 3 mmol/L MOG for 24 h on Snail accumulation in hb30-KPL cells. HSP90 was used as the loading control. (M) Effects of *ACACA* knockdown on the Matrigel invasion and migration of hb30-KPL cells (left) and indicated KL cell lines (right). (N) Effect of *CREBBP* knockdown on Matrigel invasion in hb30-KPL cells (left) and the indicated KL cell lines (right). (O) Effect of treatment with the CBP inhibitor C646 (25 μmol/L) for 24 h in the presence or absence of 10 mmol/L acetate on Matrigel invasion. All experiments were performed in duplicate unless otherwise indicated. The data are presented as mean ± SD, unless otherwise indicated. Significant differences between groups were determined by a two-sided unpaired Student's *t*-test. *P < 0.05, **P < 0.01, ***P < 0.001, *NS*: not significant. Abbreviations: CCLE, Cancer Cell Line Encyclopedia; NC, negative control; ATG5, autophagy related 5; TFEB, transcription factor EB; CAMKK2, calcium/calmodulin dependent protein kinase kinase 2; MP, methyl pyruvate; MOG, dimethyl-2-oxoglutarate; Rosi, rosiglitazone; CQ, chloroquine;TCA, tricarboxylic acid cycle; Cyto, cytoplasm; Mito, mitochondria; Rapa, rapamycin; LC3, microtubule associated protein 1 light chain 3 alpha; ACLY, ATP citrate lyase; ACSS2, acetyl-CoA synthase short chain family member 2, CS, citrate synthase; IDH1, isocitrate dehydrogenase 1; CREBBP, CREB-binding protein; ACACA, Acetyl-CoA carboxylase alpha; HSP90, heat shock protein 90

knockdown (Figure 4I), indicating that acetate should be converted to acetyl-CoA via ACSS2 to induce an invasive phenotype.

Citrate is synthesized by two independent pathways via mitochondrial CS and cytosolic IDH1 (Figure 4F) [52]. We further observed that both *CS* and *IDH1* knockdown reduced the citrate levels to a similar degree in hb30-KPL cells (Figure 4J), indicating that both the mitochondria-dependent (through CS) and mitochondria-independent routes (through IDH1) contribute to the citrate pool in KL cells. As Snail levels were also reduced by both *CS* and *IDH1* knockdown (Figure 4K), we examined whether MP (a direct substrate of CS) or MOG (a direct substrate of IDH1 and an indirect substrate of CS) could rescue the reduced Snail level. We observed that while MP did not produce a meaningful increase in Snail levels the *CS*-depleted cells, MOG rescued Snail levels in the *IDH1*-depleted cells (Figure 4K), suggesting that MOG bypassed IDH1 through the mitochondrial TCA cycle, whereas the ability of MP to bypass CS was limited. The same rescue pattern was observed with CQ treatment (Figure 4L), indicating that CQ did not affect the mitochondria-dependent MOG to citrate flux. However, even in the MOG-supplemented condition, if *ACLY* was depleted, the Snail level was not restored (Figure 4K), suggesting that citrate must be converted into acetyl-CoA via ACLY to increase Snail protein levels. Taken together, these data indicate that both acetate and citrate, independent of their synthesis routes, are sources of acetyl-CoA in KL cells and that acetyl-CoA is the key metabolite that enhances the invasion of KL cells.

We then investigated the downstream mechanisms of acetyl-CoA. Acetyl-CoA is mainly used for fatty acid synthesis and protein acetylation. To determine whether acetyl-CoA-mediated fatty acid synthesis is the main driver of cell invasion, we knocked down acetyl-CoA carboxylase alpha (*ACACA*), which may increase the level of acetyl-CoA by suppressing its conversion to malonyl-CoA [49], increased the invasion of hb30-KPL and KL cell lines (Figure 4M), indicating that fatty acid synthesis is not the main driver of the invasive phenotype. However, the knockdown of CREB-binding protein (*CREBBP*), which is involved in transferring acetyl groups from acetyl-CoA to lysine side chains of target proteins [53], reduced invasion in the hb30-KPL and KL cell lines (Figure 4N), and chemical inhibition of CBP acetyltransferase activity with C646 diminished the effect of acetate on invasion (Figure 4O, Supplementary Figure S4F). Taken together, these data indicate that activated autophagy generates precursors for acetyl-CoA, which enhances the invasiveness of KL lung cancer cells through target protein acetylation.

3.5 | Autophagy-derived acetyl-CoA enhanced KL cell invasion via CBP-mediated Snail acetylation

As the Snail level was found to be highly associated with invasiveness of KL cancer cells (Figure 1E) and concordantly changed with perturbation of citrate pathways (Figure 4K), we hypothesized that acetyl-CoA-induced invasiveness is mediated by Snail. To test this hypothesis, we first examined changes in the Snail level following changes in acetyl-CoA abundance. Both acetate supplementation and *ACACA* knockdown increased the Snail protein level without affecting its mRNA level (Supplementary Figure S5A-S5B). We further observed a concurrent increase in the acetylated Snail level upon acetate supplementation (Supplementary Figure S5C), whereas *ACLY* knockdown decreased global protein acetylation and acetylated Snail levels (Supplementary Figure S5D). In support of our hypothesis, the ACLY inhibitors BMS-303141, SB-204990 and NDI-091143 reduced Snail level and cell invasion, and co-treatment with the proteasome inhibitor bortezomib rescued BMS-303141-induced Snail depletion (Figure 5A).

Consistent with these observations, hb30-KPL cells showed increased global protein acetylation and acetylated Snail levels compared to hb30-KP cells (Figure 5B). As activated autophagy supplies acetyl-CoA in the context of *KRAS-LKB1* co-mutation, chemical inhibition of the upstream mediator CAMKK2 decreased acetylated Snail levels in hb30-KPL cells (Supplementary Figure S5E). Similarly, direct inhibition of autophagy by CQ or *siATG5/TFEB* produced the same effect (Figure 5C and D), while autophagic activation by mTOR inhibition in hb30-KP cells increased global protein acetylation (Supplementary Figure S5F), histone H3 acetylation (Supplementary Figure S5G), a representative protein responsive to the nucleocytoplasmic acetyl-CoA level [54], and Snail acetylation (Supplementary Figure S5H). Furthermore, *ACLY*-depleted hb30-KPL cells did not show elevated Snail expression upon autophagic activation (Figure 5E). Collectively, these data indicate that acetyl-CoA supplied by activated autophagy increases Snail acetylation.

We next sought to identify enzymes that mediate Snail acetylation and their roles in regulating Snail stability and invasiveness in KL cells. The acetyltransferase CBP acetylates Snail using acetyl-CoA, while HDAC class I and II enzymes deacetylate Snail [55]. Consistent with this, chemical inhibition and siRNA-mediated depletion of *CBP* (si*CREBBP*) decreased the Snail protein levels in hb30-KPL and KL cell lines, and this effect was partially due to a decrease in protein stability, as evidenced by the
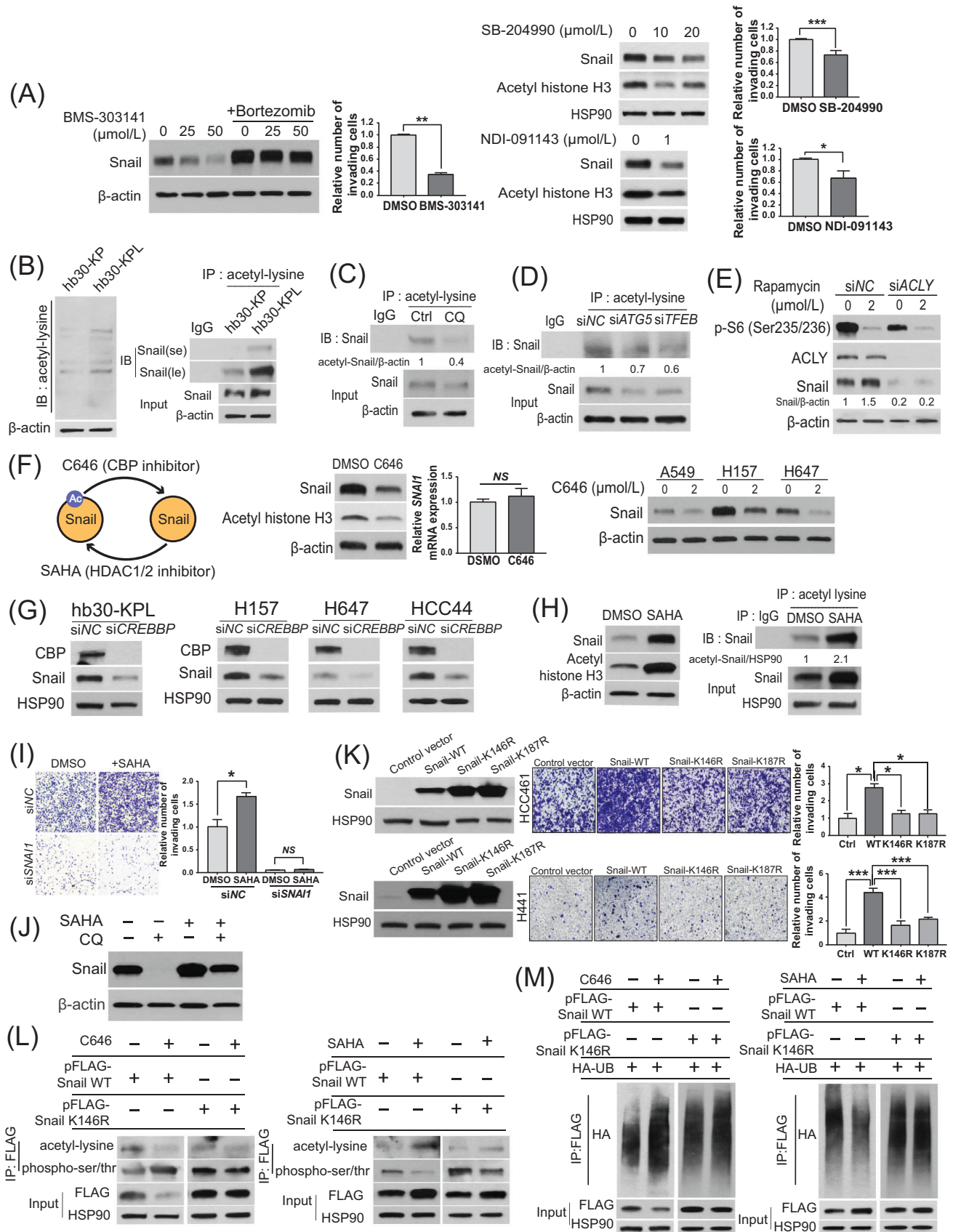
FIGURE 5 Autophagy-derived acetyl-CoA enhances KL cell invasion via CBP-mediated Snail acetylation. (A) Effect of exposure to BMS-303141, NDI-091143 and SB-204990 (ACLY inhibitor) at the indicated concentrations for 24 h, 24 h, and 2 h in the presence or absence of 20 nmol/L bortezomib for the last 3 hours (BMS-303141) on Snail protein accumulation in hb30-KPL cells, as determined by Western blotting.

lack of obvious change in Snail mRNA levels (Figure 5F and G), while the HDAC inhibitor SAHA increased acetylated Snail levels (Figure 5H) and cell invasion, which was reversed by *SNAI1* knockdown (Figure 5I), indicating that the increase in cell invasion induced by HDAC inhibition is Snail-dependent. In addition, the treatment of hb30-KPL cells with cycloheximide, which inhibits protein synthesis, reduced the Snail protein levels, but this effect was partially reversed by treatment with SAHA (Supplementary Figure S5I), suggesting that Snail stabilization was at least partially mediated by Snail acetylation. Moreover, Snail depletion induced by CQ was rescued by SAHA (Figure 5J), further indicating that autophagy drives Snail acetylation. We observed that the K cells expressing acetylation-deficient Snail mutants (Snail-K146R and Snail-K187R) showed significantly lower invasiveness than the Snail-WT cells (Figure 5K), indicating that Snail acetylation confers invasiveness in KL cells. The reduced acetylation of wild-type Snail induced by the CBP inhibitor C646 increased Snail phosphorylation, accompanied by increased polyubiquitination (Figure 5L and M, left), while the increased acetylation of wild-type Snail induced by SAHA decreased Snail phosphorylation, accompanied by decreased polyubiquitination (Figure 5L and M, right). Moreover, C646 or SAHA impacted the phosphorylation or acetylation of Snail K146R to a lesser degree than that of wild-type Snail (Figure 5L and M). Taken together, these data indicate that acetyl-CoA produced by autophagy enhances the invasion of KL cells via CBP-mediated Snail acetylation.

Beta-actin and HSP90 were used as the loading controls (left panels). Acetyl histone H3 was used as a control to represent intracellular acetyl-CoA levels. The effect of exposure of hb30-KPL cells to 50 μmol/L BMS-303141 for 24 h, 1 μmol/L NDI-091143 for 24 h and 20 μmol/L SB-204990 for 2 h on Matrigel invasion. Quantified data of cells that invaded through Matrigel-coated Transwell membranes are shown in the right panels. The bar plots show the mean ± SD of three independent experiments. (B) Steady-state levels of total protein acetylation in hb30-KP and hb30-KPL cells (left) and immunoprecipitation-Western blotting analysis of acetylated Snail levels in hb30-KP and hb30-KPL cells (right). Beta-actin was used as the loading control. se, short exposure; le, long exposure. (C-D) Immunoprecipitation-Western blotting analysis of acetylated Snail levels upon treatment with 50 μmol/L CQ for 24 h (C) or *ATG5* or *TFEB* knockdown (D) in hb30-KPL cells. Values obtained from a quantitative densitometric analysis of acetylated Snail relative to beta-actin are shown underneath the Snail blots. (E) The effect of 2 μmol/L rapamycin (for 5 h) with or without *ACLY* knockdown on Snail protein accumulation was assessed by Western blotting analysis. Values obtained from a quantitative densitometric analysis of acetylated Snail relative to beta-actin are shown underneath the Snail blots. (F) Effect of the CBP inhibitor C646 (25 μmol/L) for 2 h on the levels of the indicated proteins in hb30-KPL (left) and KL cell lines (right), as determined by Western blotting. Real-time PCR analyses of relative *SNAI1* gene expression in hb30-KPL cells after exposure to 25 μmol/L C646 for 2 h (middle; 2 RNA samples). The schematic shows the modes of action of the tested compounds. (G) The effects of hb30-KPL (left) and KL cell line (right) treatment with *CREBBP*-specific siRNA for 72 h on Snail protein accumulation were assessed by Western blotting analysis. HSP90 was used as the loading control. (H) Effect of the 3 μmol/L HDAC inhibitor SAHA for 15 h on the levels of the indicated proteins in hb30-KPL cells (left). Immunoprecipitation-Western blotting analysis of acetylated Snail levels in hb30-KPL cells upon treatment with 3 μmol/L SAHA for 15 h (right). Beta-actin and HSP90 were used as the loading controls. Values obtained from a quantitative densitometric analysis of acetylated Snail relative to HSP90 are shown underneath the Snail blots. (I) Matrigel invasion assay of hb30-KPL cells with *SNAI1* knockdown with or without 3 μmol/L SAHA treatment for the last 15 h. Representative bright-field micrographs (20×) of cells that invaded through Matrigel-coated Transwell membranes are shown in the left panel, and quantification data of invaded cell numbers are shown in the right panel. (J) The effect of exposure of hb30-KPL cells to a combination of 3 μmol/L SAHA and 50 μmol/L CQ for 24 h on Snail protein accumulation was assessed by Western blotting. Beta-actin was used as the loading control. (K) The effects of ectopic expression of wild-type or acetylation-deficient Snail (K146R or K187R) on Snail protein levels in the indicated K cell lines were determined by Western blotting analysis at 24 h post-transfection. HSP90 was used as the loading control (left). Representative images of Matrigel invasion under the above conditions are shown in the middle panels, and quantified data are shown in the right panels. (L) Immunoprecipitation-Western blotting analysis of phosphorylated/acetylated Snail in A549 cells transfected with wild-type Snail (pFLAG-Snail WT) or an acetylation-deficient Snail mutant (pFLAG-SnailK146R) with or without 25 μmol/L C646 treatment for 2 h (left) or 3 μmol/L SAHA treatment for 5 h (right). Flag was immunoprecipitated from 1-μg samples of cell lysates with 40 μL of anti-Flag M2 Affinity gel and Western blotted with the indicated antibodies. HSP90 was used as the loading control. Phospho-Ser/Thr, phosphorylated serine/threonine. (M) Immunoprecipitation-Western blotting for analysis of polyubiquitinated Snail in A549 cells co-transfected with HA-ubiquitin and wild-type Snail (pFLAG-Snail WT) or an acetylation-deficient Snail mutant (pFLAG-SnailK146R) with or without 25 μmol/L C646 treatment for 2 h (left) or 3 μmol/L SAHA treatment for 5 h (right). Flag was immunoprecipitated from 1-μg samples of cell lysates with 40 μL of anti-Flag M2 Affinity gel and Western blotted with the indicated antibodies. HSP90 was used as the loading control. All experiments were performed in duplicate unless otherwise indicated. The data are presented as mean ± SD, unless otherwise indicated. Significant differences between groups were determined by a two-sided unpaired Student's *t*-test. *$P < 0.05$, **$P < 0.01$, ***$P < 0.001$, *NS*: not significant. Abbreviations: ACLY, ATP citrate lyase; HSP90, heat shock protein 90; DMSO, dimethyl sulfoxide; CQ, chloroquine; NC, negative control; ATG5, autophagy related 5; TFEB, transcription factor EB;; HDAC, histone deacetylase; SAHA, suberoylanilide hydroxamic acid; PCR, polymerase chain reaction; CREBBP, CREB Binding Protein; IB, immunoblot; IP, immunoprecipitation; HA, hemagglutinin; UB, ubiquitin

3.6 | Elevated TFEB acetylation triggered a positive feedback loop to activate autophagy

The enhanced CLEAR activity in KL cells was unexpected because mTORC1, which is activated due to *LKB1* loss in the KL background [31], is known to suppress CLEAR activity through inhibitory phosphorylation of TFEB [44, 56, 57]. Thus, we speculated that enhanced CLEAR activity in KL cells might be associated with acetylation of TFEB. To examine the effect of TFEB acetylation on its transcriptional regulatory activity, we overexpressed wild-type TFEB and acetylation-deficient TFEB[4KR] mutant and measured CLEAR activity. Indeed, the expression of the acetylation-deficient TFEB[4KR] mutant significantly reduced CLEAR activity measured by luciferase reporter assays in hb30-KPL cells (Figure 6A, left). Furthermore, the TFEB activity levels in the hb30-KPL cells expressing the TFEB[4KR] mutant were less responsive to SAHA treatment than those in the cells expressing wild-type TFEB (Figure 6A, right). These data indicate that acetylation contributes to TFEB activation in the context of active mTORC1.

Considering that global protein acetylation was increased in hb30-KPL cells (Figure 5B), we hypothesized that high acetyl-CoA levels may also promote TFEB acetylation, overriding the negative regulatory effect of mTORC1 and resulting in increased activity of the autophagy-lysosomal pathway. In support of this hypothesis, although we observed a higher level of TFEB phosphorylation at Ser211 in hb30-KPL cells than in hb30-KP cells, the level of acetylated TFEB was also higher in hb30-KPL cells (Figure 6B). To further investigate the consequences of these seemingly conflicting compound modifications of TFEB, we compared the localization of TFEB between hb30-KP and hb30-KPL cells. Intriguingly, hb30-KPL cells showed a higher level of nuclear-translocated TFEB (Figure 6C), which was in accordance with the increased CLEAR activity (Figure 3C). Consistent with these data, both acetate and SAHA increased the level of nuclear TFEB (Figure 6D) and CLEAR activity (Figure 6E) and increased autophagic flux in hb30-KPL cells, as shown by the increased CQ+/CQ− LC3-II ratio in the LC3 turnover assay (Figure 6F) and the increased number of both autophagosomes (mRFP+/GFP+) and autolysosomes (mRFP+/GFP−) in the mRFP-GFP-LC3 lysosome delivery assay (Figure 6G). Notably, both acetate and SAHA also increased the acetylated TFEB, phosphorylated TFEB and total TFEB protein levels without significantly changing the TFEB mRNA level (Figure 6H–J), suggesting that acetylated TFEB is protected from proteasomal degradation. The

constant phospho-RPS6 (p-S6) level under acetate and SAHA treatment further indicated that the increase in phosphorylated TFEB was independent of mTORC1 activity (Figure 6H and I).

As TFEB phosphorylation and acetylation occur simultaneously (Figure 6B, H and I), we modulated each modification in different ways and evaluated changes in TFEB activity by CLEAR luciferase assays. We observed a decrease in the acetylated TFEB level in response to *ACLY* knockdown in hb30-KPL cells (Figure 6K, lower left). Under this condition, rapamycin, which inhibits TFEB phosphorylation, did not rescue CLEAR activity (Figure 6K, lower right). In contrast, calcineurin inhibition (a phosphatase recognizing TFEB [58]) by FK506 decreased CLEAR activity by increasing the level of phospho-TFEB in hb30-KPL cells (Figure 6L, left). Under these conditions, both acetate and SAHA treatment overcame the effect of FK506, resulting in increased CLEAR activity (Figure 6L, right). Collectively, these data suggest that while phosphorylation mainly functions by regulating TFEB activity through cytosolic retention as opposed to nuclear translocation, acetylation controls TFEB function by stabilizing it to resist proteasomal degradation, resulting in simultaneous increases in both active (nuclear) and nonactive (cytosolic) TFEB levels. As the former is dominant over the latter in terms of TFEB activity [56], enhanced TFEB acetylation may activate the autophagy-lysosomal pathway even when TFEB phosphorylation increases.

Next, we examined whether autophagic inhibition disrupts this positive feedback loop. STO-609 effectively reduced acetylated TFEB levels (Figure 6M). Conversely, acetate and SAHA partially rescued the reduction in TFEB protein levels under CQ treatment (Figure 6N). These results are consistent with previous observations that TFEB acetylation was involved in maintaining the total TFEB protein level (Figure 6H–J). Taken together, these results indicate that autophagy-supplied acetyl-CoA contributes to further autophagic activation through TFEB acetylation.

3.7 | The autophagy/acetyl-CoA/acetyl-Snail axis underlied the enhanced invasion of KRAS-mutated pancreatic cancer cells

KRAS-mutated pancreatic ductal adenocarcinoma is characterized by increased dependence on autophagy and macropinocytosis [59]. Thus, we hypothesized that our model may be applicable for *KRAS*-mutated pancreatic cancer cell lines with physiological characteristics similar to those of KL lung cancer cell lines.
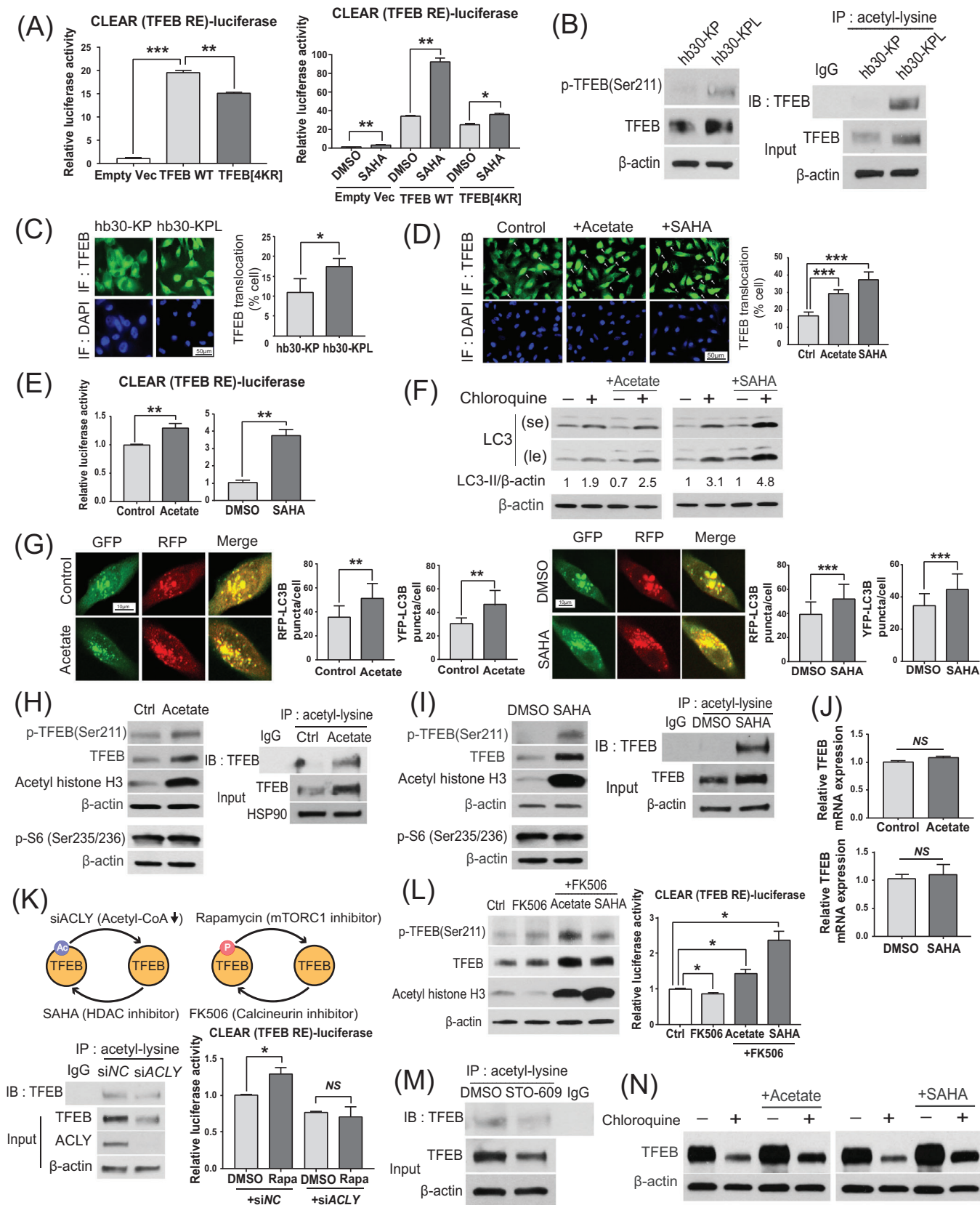
FIGURE 6 Elevated TFEB acetylation triggers a positive feedback loop to activate autophagy. (A) Effect of ectopic expression of wild-type TFEB or acetylation-deficient TFEB[4KR] for 24 h on the relative luciferase activity in hb30-KP cells transiently co-transfected with a CLEAR motif-driven luciferase reporter construct (left). Relative luciferase activity after the addition of 3 μmol/L SAHA for the last 5 h under identical conditions (right). (B) Steady-state levels of TFEB and phospho-TFEB (Ser211) in hb30-KP and hb30-KPL cells, as determined

As expected, citrate levels were significantly higher in 41 pancreatic cancer cell lines than in 710 non-pancreatic and non-lung cancer cell lines based on CCLE metabolomic data [47] (Supplementary Figure S6A). Autophagic inhibition by CQ effectively reduced acetyl-CoA levels, total/acetylated Snail levels, and cell invasion (Supplementary Figure S6B-S6E). This hypothesis was further supported by the observation of reduced Snail expression and invasion upon *ACLY* knockdown (Supplementary Figure S6F-S6G). Finally, we observed that pancreatic cancer cells expressing an acetylation-deficient Snail mutant (Snail-K146R or Snail-K187R) showed reduced invasiveness compared to cells expressing wild-type Snail (Supplementary Figure S6H-S6I). Thus, the autophagy/acetyl-CoA/acetyl-Snail axis was also observed in *KRAS*-mutated pancreatic cancer cell lines.

3.8 | The autophagy/acetyl-CoA/acetyl-Snail axis was validated in tumor tissues, and pharmacological inhibitors suppressed the metastasis of KL cells in vivo

Finally, we clinically validated the autophagy/acetyl-CoA/acetyl-Snail axis using a LUAD patient TMA with associated survival data. Consistent with the findings from the analysis of large-scale gene expression-based cohort data (TCGA, GSE72094, and GSE41271) (Figure 1D, Supplementary Figure S1E), the high intensities of both nuclear Snail and total Snail were significantly associated with poor overall survival in the TMA cohort (Figure 7A, Supplementary Figure S7A). Moreover, tumor tissues with higher nuclear Snail or total Snail intensities showed significantly higher LAMP2 (a marker of autolysosomes [60]), nuclear acetyl-lysine (a marker of nuclear

by Western blotting (left) and immunoprecipitation-Western blotting analysis of acetylated TFEB in hb30-KP and hb30-KPL cells (right). Beta-actin was used as the loading control. (C) Detection of steady-state TFEB expression in hb30-KP and hb30-KPL cells by immunofluorescence (scale bar, 50 μm). Analyses were performed with anti-TFEB antibody (green). DAPI was used to visualize nuclei (left). The bar plots show the numbers of hb30-KP and hb30-KPL cells with nuclear TFEB (four independent experiments, right). (D) Detection of TFEB expression in hb30-KPL cells upon treatment with 10 mmol/L acetate for 24 h or 3 μmol/L SAHA for 5 h by immunofluorescence (scale bar, 50 μm). Analyses were performed with anti-TFEB antibody (green). DAPI was used to visualize nuclei. Arrows indicate cells with nuclear-localized TFEB. (left). The bar plots show the number of hb30-KPL cells with nuclear TFEB (four independent experiments, right). (E) Effect of treatment with 10 mmol/L acetate for 24 h or 3 μmol/L SAHA for 5 h on relative luciferase activity in hb30-KPL cells stably transfected with a CLEAR motif-driven luciferase reporter construct. The bar plots show the mean $\pm$ SD of three (left panel) and two (right panel) independent experiments. (F) The influence of treatment with 10 mmol/L acetate for 24 h or 3 μmol/L SAHA for 5 h with or without 50 μmol/L CQ for the last 3 h on LC3-II accumulation in hb30-KPL cells was assessed by Western blotting. Beta-actin was used as the loading control. Values obtained from a quantitative densitometric analysis of LC3-II relative to beta-actin are shown underneath the LC3 blots. se, short exposure; le, long exposure. (G) mRFP-GFP-LC3 lysosome delivery assay in hb30-KPL cells in response to 10 mmol/L acetate for 24 h (left) or 3 μmol/L SAHA treatment for 15 h (right). Representative GFP-LC3, RFP-LC3 and overlay images are shown. The number of red puncta (mRFP+/GFP−) and yellow puncta (mRFP+/GFP+) per cell was quantified (15–30 cells/treatment). (H) The effect of exposure of hb30-KPL cells to 10 mmol/L acetate for 24 h on the accumulation of the indicated proteins was determined by Western blotting. Beta-actin was used as the loading control (left). Immunoprecipitation-Western blotting analysis of acetylated TFEB under the same conditions in hb30-KPL cells (right). (I) The effect of exposure of hb30-KPL cells to 3 μmol/L SAHA for 18 h on the accumulation of the indicated proteins was determined by Western blotting. Beta-actin was used as the loading control (left). Immunoprecipitation-Western blotting analysis of acetylated TFEB under identical conditions in hb30-KPL cells (right). (J) Real-time PCR analyses of relative *TFEB* gene expression in hb30-KPL cells exposed to 10 mmol/L acetate (2 RNA samples) for 24 h or 3 μmol/L SAHA (3 RNA samples) for 5 h. (K) Immunoprecipitation-Western blotting analysis of acetylated TFEB upon *ACLY* knockdown in hb30-KPL cells (lower left). The effect of 2 μmol/L rapamycin (for 5 h) with or without *ACLY* knockdown on relative luciferase activity in hb30-KPL cells stably transfected with a CLEAR motif-driven luciferase reporter construct (lower right). The schematic in the upper panel shows the mode of action of the tested compounds. (L) The effect of exposure of hb30-KPL cells to 1 μmol/L FK506 (last 1 h) with or without 10 mmol/L acetate and 3 μmol/L SAHA for 15 h on the accumulation of the indicated proteins was determined by Western blotting (left). Beta-actin was used as the loading control. The relative luciferase activity in hb30-KPL cells stably transfected with a CLEAR motif-driven luciferase reporter construct was measured under the same conditions (right). (M) Immunoprecipitation-Western blotting analysis of acetylated TFEB in hb30-KP cells upon treatment with 50 μmol/L STO-609 for 24 h. Beta-actin was used as the loading control. (N) The effect of exposure of hb30-KPL cells to a combination of 10 mmol/L acetate or 3 μmol/L SAHA and 50 μmol/L CQ for 24 h on TFEB protein accumulation was determined by Western blotting. Beta-actin was used as the loading control. All experiments were performed in duplicate unless otherwise indicated. The data are presented as mean $\pm$ SD, unless otherwise indicated. Significant differences between groups were determined by a two-sided unpaired Student's *t*-test. *$P < 0.05$, **$P < 0.01$, ***$P < 0.001$, *NS*: not significant. Abbreviations: TFEB, transcription factor EB; CLEAR, coordinated lysosomal expression and regulation; TFEB RE, TFEB reporter; DAPI, 4′,6-diamidino-2-phenylindole; SAHA, suberoylanilide hydroxamic acid; CQ, chloroquine; mRFP, monomeric red fluoresecnct protein; GFP, green fluorescent protein; LC3B, microtubule-associated protein 1A/1B-light chain 3B; PCR. polymerase chain reaction; IP, immunoprecipitation; IB, immunoblot; Rapa, Rapamycin; ACLY, ATP citrate lyase; HDAC, histone deacetylase; HSP90, heat shock protein 90; DMSO, dimethyl sulfoxide
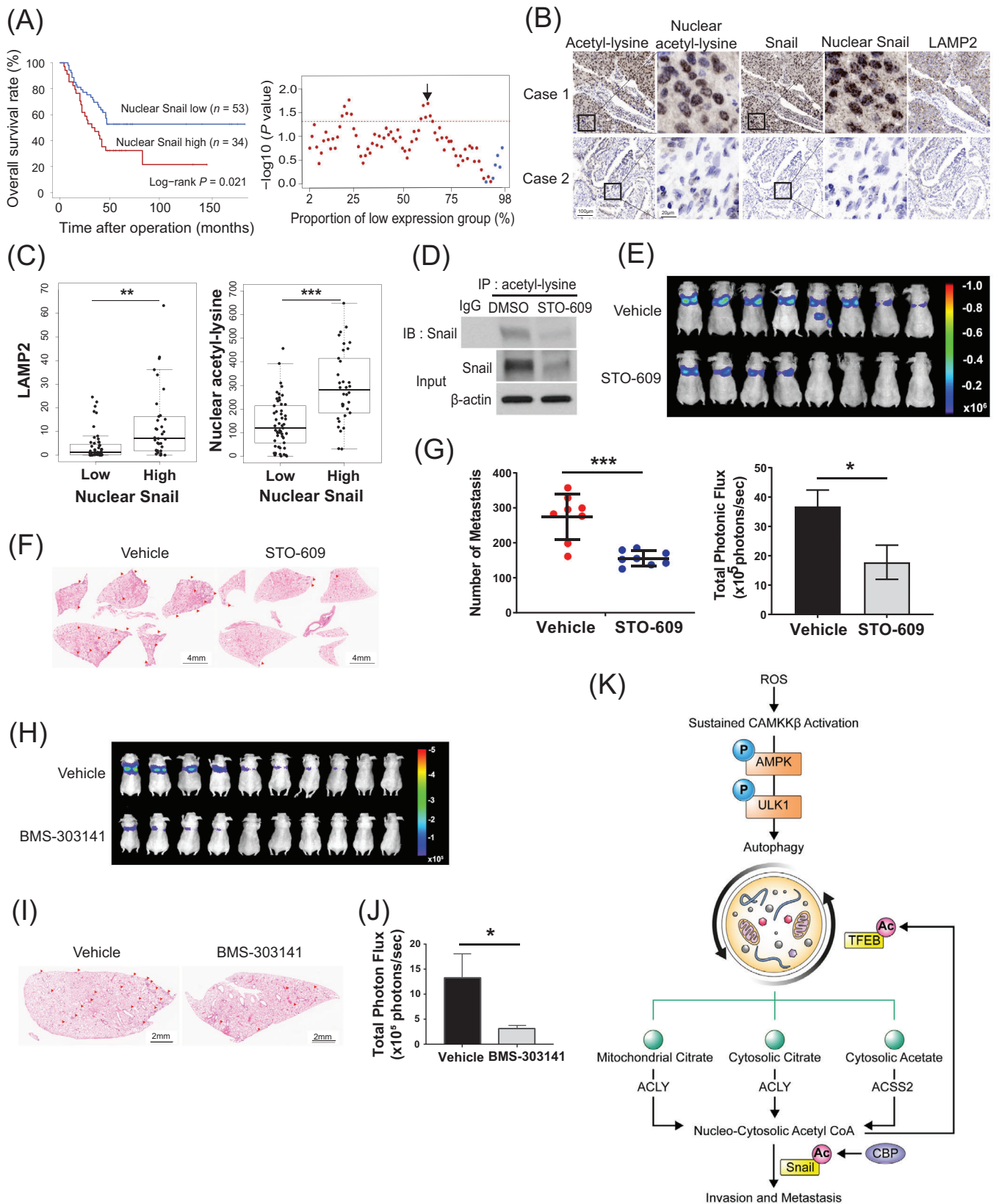
FIGURE 7 The autophagy/acetyl-CoA/acetyl-Snail axis is validated in tumor tissues, and pharmacological inhibitors suppress the metastasis of KL cells in vivo. (A) The prognostic effect of nuclear Snail level in a LUAD tissue microarray. Patients were classified into two groups based on the nuclear Snail protein expression score (multiplying the percentage and the median intensity of positively stained cells). The X-axis in the plot indicates the varying threshold of Snail protein expression score. Differences in survival between the low and high

acetyl-CoA), and total acetyl-lysine (a marker of intracellular acetyl-CoA [61]) intensities (Figure 7B and C, Supplementary Figure S7B), indicating that the autophagy/acetyl-CoA/acetyl-Snail axis is intact in human lung tumor tissues.

To evaluate the pro-metastatic role of the autophagy/acetyl-CoA/acetyl-Snail axis in vivo, we used an experimental mouse model of metastasis in which lung metastasis was induced by tail vein injection of luciferase-expressing A549 (KL background) cells [62]. Based on our observations that CAMKK2 inhibition effectively attenuated 2D invasion by reducing autophagic flux and acetyl-CoA levels in hb30-KPL cancer cells (Supplementary Figures S3A-S3B, S4D, and Figure 4C), we first evaluated CAMKK2 as an anti-metastatic target. We confirmed that STO-609 effectively decreased the level of acetylated Snail in the A549-luc cell line in vitro (Figure 7D). The mice in the STO-609 treatment groups showed a reduced total metastatic burden (Figure 7E) as well as a significant reduction in the number of lung metastases compared to the mice in the vehicle-treated group (Figure 7F and G). We further found that Snail-expressing cells in metastatic tumor foci were commonly observed in the vehicle-treated group, whereas they were rare in the STO-609-treated group (Supplementary Figure S7C). Also, we found that the ACLY inhibitor BMS-303141 robustly reduced the total metastatic burden (Figure 7H–J). These results indicate that inhibition of the autophagy/acetyl-CoA axis consistently demonstrated an anti-metastatic effect in vivo.

Taken together, the study results indicated that autophagy-derived acetyl-CoA and subsequent Snail acetylation are the key mechanisms of metastasis and aggressive behavior not only in KL lung cancer but also possibly in other autophagy-activated tumor types, including pancreatic cancer (Figure 7K). Furthermore, pharmacological inhibition of this axis could be a promising therapeutic strategy for various metastatic tumors.

4 | DISCUSSION

Using lung cancer cell line models and tumor specimens, we demonstrated that enhanced autophagy in KL cancers

nuclear Snail protein expression score groups were estimated by the log-rank test. The dashed line indicates a *P* value < 0.05. The red and blue circles indicate hazard ratios of >1 (high nuclear Snail protein expression score group with worse prognosis) and ≤1 (high nuclear Snail protein expression score group with better prognosis), respectively (right). Kaplan-Meier estimates of overall survival after surgical resection in 87 patients with LUAD divided into low and high nuclear Snail expression groups (left) defined by the arrowhead in the right panel. Comparison of survival was based on the log-rank test. (B) Total and nuclear acetyl-lysine, total and nuclear Snail, and LAMP2 protein levels in 87 LUAD tissues were analyzed by IHC. Representative IHC images from two tumor tissues are shown. Scale bars, 20 μm and 100 μm. (C) Comparison of nuclear acetyl-lysine and LAMP2 expression measured by quantification of IHC analysis between the groups with high and low nuclear Snail levels defined in Figure 7A. *P* values were calculated with a two-sided unpaired Wilcoxon rank-sum test. The numbers of samples in the low and high nuclear Snail expression groups were 53 and 34, respectively. The box-and-whisker plots show the medians (middle line), first quartiles (lower bound line), third quartiles (upper bound line) and ±1.5× interquartile ranges (whisker lines); the raw data are overlaid. (D) Immunoprecipitation-Western blotting analysis of acetylated Snail in the A549-luc cell line after treatment with 50 μmol/L STO-609 for 24 h. Beta-actin was used as the loading control. (E) Effect of STO-609 on tumor metastasis in the A549-luc tail vein injection model. A549-luc cells were intravenously injected into nude mice (8 mice per group). The mice were treated with vehicle or STO-609 (100 mg/kg) for 28 days beginning on the day of cell injection. Bioluminescence images of each group at 4 weeks post-injection are shown. The data are presented as the mean ± SEM values. (F) Representative images of H&E staining of lung sections from the vehicle and STO-609 treatment groups are shown. Red arrows in lung lobes point to metastatic nodules. Scale bars, 4 mm. (G) Number of lung metastatic nodules (left) and total metastatic burden, represented by total photonic flux (right) in the vehicle and STO-609 treatment groups. Data are shown as the mean ± SD and mean ± SEM, respectively. (H) Effect of BMS-303141 on tumor metastasis in the A549-luc tail vein injection model. A549-luc cells were intravenously injected into nude mice (10 mice per group). The mice were treated with vehicle or BMS-303141 (100 mg/kg) for 20 days beginning on the day of cell injection. Bioluminescence images of each group at 3 weeks post-injection are shown. (I) Representative images of H&E staining of lung sections from the vehicle and BMS-303141 treatment groups are shown. Red arrows in lung lobes indicate metastatic nodules. Scale bars, 2 mm. (J) The total metastatic burden was estimated by measuring the photon flux. The data are presented as the mean ± SEM values. (K) Proposed model of autophagy-derived tumor metastasis in lung cancer. ROS induces CAMKK2-AMPK-dependent autophagy in *LKB1*-deficient *KRAS*-mutated lung cancer cells. Acetyl-CoA supplied by autophagy drives invasion and metastasis through Snail acetylation. Acetyl-CoA is further used to acetylate the TFEB protein, creating a positive feedback loop to sustain high levels of autophagy. Significant differences between groups were determined by a two-sided unpaired Student's *t*-test. *P < 0.05, **P < 0.01, ***P < 0.001. Abbreviations: LUAD, lung adenocarcinoma; LAMP2, lysosomal Associated Membrane Protein 2; IP, immunoprecipitation; IB, immunoblot; DMSO, dimethyl sulfoxide; SEM, standard error of the mean; H&E, hematoxylin and eosin; LKB1, liver kinase B1; ROS, reactive oxygen species; CAMKK2, calcium/calmodulin-dependent protein kinase kinase 2; AMPK, AMP-activated protein kinase; ULK1, unc-51 like autophagy activating kinse 1; TFEB; transcription factor EB; ACLY, ATP citrate lyase; ACSS2, acly-coa synthetase short chain family member 2; CBP, CREB binding protein

supplied intracellular citrate and acetyl-CoA, thereby facilitating cancer cell invasion and metastasis through the CBP-dependent activation of Snail acetylation. Furthermore, using lung tumor tissues, we showed that patients with short overall survival exhibited elevated levels of LAMP2, acetyl-lysine and nuclear Snail. Concurrent TFEB acetylation created a positive feedback loop to maintain elevated autophagic flux by overcoming negative regulation by mTORC1. Inhibition of the autophagy/acetyl-CoA axis by targeting CAMKK2 or ACLY effectively reduced invasion and metastasis in vitro and in vivo. We also demonstrated that the autophagy/acetyl-Snail axis was preserved in oncogenic *KRAS*-driven pancreatic cancers, where, similar to KL lung cancers, autophagy was elevated and required for tumor progression [63]. Conceptually, these findings advanced our understanding of the mechanisms of how autophagy in early metastatic cancers contributes to EMT activation.

Recent studies have indicated that autophagy was upregulated during metastasis, as evidenced by increased punctate staining or expression of microtubule associated protein 1 light chain 3 beta (LC3B) in various metastatic tumors [64–68]. However, how these tumors utilize autophagy to promote EMT and metastasis is largely unknown. Metastatic cancer cells increase ATP synthesis to support motility by augmenting mitochondrial activity and promoting catabolic metabolism, including autophagy [69, 70]. A more direct connection between autophagy and EMT activation has been demonstrated in hepatocellular carcinoma, where autophagy was required for transforming growth factor-β (TFG-β)-induced EMT [71], and during invasion of a RAS-transformed cancer cell line, where autophagy was required for the production of the pro-invasive cytokines interleukin-6 (IL-6), matrix metalloproteinase-2 (MMP-2) and Wnt family member 5A (WNT5A) [72]. Very recently, Yamamoto et al. [73] demonstrated that autophagy degraded major histocompatibility complex class I (MHC-I) in pancreatic cancer to promote immune evasion. The present study first uncovered a direct regulatory mechanism of autophagy for the EMT transcription factor Snail. Snail plays an essential role in migration, metastasis, relapse, and immune evasion via various mechanisms [9, 55, 74–80]. However, Snail was highly unstable with a short half-life mediated by phosphorylation by GSK3β [81] and polycystin 1 (PKD1) [82] or by direct binding with E3 ligases, such as F-box and leucine rich repeat protein 14 (FBXL14) [83]. We demonstrated that autophagy-derived acetyl-CoA acetylates Snail, thereby blocking its inhibitory phosphorylation and subsequent proteasomal degradation. This finding was in line with previous reports indicating that Snail acetylation increased its stability by suppressing its ubiquitination [55, 83, 84]. The present study newly identified autophagy

as a main supplier of metabolite precursors of acetyl-CoA needed for Snail acetylation and provided alternative reversal strategies either by suppressing the upstream autophagy-inducing kinase CAMKK2 or by inhibiting the downstream acetyl-CoA producer ACLY.

Increasing evidence indicates that autophagy is tightly coupled to mitochondrial function [85–88]. Moreover, cytosolic citrate, an immediate precursor of acetyl-CoA, is mainly supplied by mitochondria. Thus, it is important to determine whether the increased acetyl-CoA in KL cells is directly attributed to mitochondria rather than autophagy. Our data indicated that cell-permeable MP or MOG, two major carbon sources for citrate biosynthesis in mitochondria-dependent and mitochondria-independent manners, respectively (Figure 4F), rescued citrate levels in the presence of CQ, while the PPARγ agonist rosiglitazone, which facilitates mitochondrial biogenesis, did not (Figure 4D). These data demonstrated that KL cancer cells depended on autophagy to supply metabolites for acetyl-CoA synthesis rather than directly activating mitochondrial function or increasing mitochondrial mass. Moreover, mitochondria-dependent Snail rescue was observed even under autophagic inhibition conditions (Figure 4L), indicating that mitochondria were still functional upon autophagic inhibition, thus supporting the pro-metastatic function of autophagy.

Our data indicated that the autophagy-driven increase in acetyl-CoA established a positive feedback loop of autophagic activation through TFEB acetylation. TFEB is a master regulator of lysosomal function and autophagy. TFEB is phosphorylated by mTORC1, resulting in cytosolic retention and decreased transcriptional activity of CLEAR network genes [56, 57]. The increased CLEAR network activity observed despite increased mTORC1 signaling as a consequence of *LKB1* loss led us to hypothesize that an additional mTORC1-independent pathway regulated TFEB in the KL context. In this regard, we postulated that acetylation, another post-translational modification that enhances TFEB transcriptional activity [89], might underlie this seemingly paradoxical observation. This study demonstrated that TFEB acetylation increased the stability of total TFEB (both phosphorylated and dephosphorylated forms), thereby resulting in elevated levels and activity of nuclear TFEB. This finding may explain how these metastatic tumors had sustained autophagic activity. If so, one potential method to blunt this pro-metastatic autophagy is to disrupt the acetyl-CoA supply, thereby restoring mTORC1-mediated inhibition of TFEB activity. Further study is needed to elucidate the mechanism by which acetylation increases TFEB stability. One possibility is that acetylation of TFEB may inhibit its targeting by E3 ubiquitin ligases and subsequent proteasomal degradation. In support of this hypothesis, a recent study demonstrated that

that TFEB was also degraded via the ubiquitin-proteasome pathway by binding to the STUB1 chaperone-dependent E3 ubiquitin ligase [90].

Due to the low probability of overlapping targetable alterations [e.g., epidermal growth factor receptor (EGFR), anaplstic lymphoma receptor tyrosine kinase (ALK), ROS proto-oncogene 1, receptor tyrosine kinase (ROS1), B-Raf proto-oncogene (BRAF) V600E, MET exon 14, and neutrophic receptor tyrosine kinase (NTRK)], the presence of *KRAS* mutations identified patients who are unlikely to benefit from further molecular testing [91]. Although immune checkpoint inhibitor-induced tumor regression was recently observed in a group of patients with *KRAS* mutations [92], patients with NSCLC harboring mutations in both *KRAS* and *LKB1* exhibited resistance to immunotherapy [8]. Likewise, we observed that the KRAS G12C inhibitor AMG-510 exhibited limited cytotoxicity and aberrantly facilitated Matrigel invasion through Snail upregulation in KL cells. Based on our findings that STO-609 (a CAMKK2 inhibitor) and BMS-303141 (an ACLY inhibitor) effectively reduced tumor metastasis in vivo, we speculated that these agents complement existing treatment modalities for KL lung cancer and beyond. Of these, CAMKK2 inhibitors, to the best of our knowledge, have not been evaluated in clinical trials as anticancer agents. Importantly, *CAMKK2*-knockdown mice displayed no gross physical or behavioral abnormalities [93, 94], suggesting that targeting CAMKK2 may have a high safety margin. To date, CAMKK2 inhibitors have been mainly investigated for the treatment of metabolic diseases, such as nonalcoholic fatty liver disease, neurological diseases, and skeletal diseases [95, 96]. Thus, repositioning this drug as an anti-metastatic agent might be clinically very attractive.

We expect that a CAMKK2 inhibitor may be applicable as adjuvant therapy in high-risk patients after surgical resection to prevent metastasis or as combination therapy with classical cytotoxic anticancer drugs. More specifically, we propose that the utility of CAMKK2 inhibitors is threefold. First, we believe that CAMKK2 inhibitors could be used as neoadjuvant or adjuvant therapies in early-stage cancer patients who have a high risk of metastasis and recurrence based on characteristics such as margin positivity, vascular invasion, wedge resection, tumors > 4 cm, visceral pleural involvement, and unknown lymph node status (defined as the high-risk group according to NCCN guidelines) [91]. The current regimen for this group is platinum-based therapy [91]. Considering the results of the 3D invasion assay (Figure 2O) and in vivo experimental metastasis model (Figure 7E–G), we speculated that CAMKK2 inhibitors would effectively block the initiation of invasion, aiding in the acquisition of safe surgical margins or reducing the metastasis of postsur-gical residual tumors. Furthermore, we expect that the combination of CAMKK2 inhibitors with platinum-based drugs would be feasible without additive cytotoxicity. Second, we believe that CAMKK2 inhibitors could be used in the advanced metastatic patient group. The current therapeutic strategy for this patient group is a combination of platinum-based drugs, pemetrexed and pembrolizumab (a PD-1 inhibitor). Although immunotherapy is ineffective in KL tumors [8], combination treatment with CAMKK2 inhibitors might overcome the resistance via cancer cell autonomous suppression of EMT programs as well as activation of CD8+ T cells in the tumor microenvironment based on a recent report indicating that CAMKK2 signaling in tumor-associated macrophages suppressed T cell antitumor activity [97]. The anti-metastatic effect demonstrated in this study may also affect circulating tumor cells, the cellular origin of micrometastasis, which also relied on activated autophagy to survive [98]. Furthermore, a CAMKK2 inhibitor is believed to have a novel impact on reducing resistance to platinum- and taxane-based current chemotherapy, which was driven by Snail via various mechanisms [99]. Therefore, the combination of a CAMKK2 inhibitor with other chemotherapeutic agents and immune checkpoint blockade may effectively induce the regression of colonized solid tumors (both primary and metastatic tumors). Third, we believe that CAMKK2 inhibitors could be effective in combination with KRAS G12C inhibitors, particularly for KL tumors. KRAS G12C inhibitors, such as AMG-510 and MRTX849, are currently showing clinical promise in *KRAS* G12C NSCLCs; however, approximately half of patients showed a poor clinical response [100]. Related to this finding, Adachi et al. [101] revealed that EMT was a cause of both intrinsic and acquired resistance to KRAS G12C inhibitors in NSCLC. As Snail drives EMT, we speculated that elevated activity of the autophagy/acetyl-CoA/acetyl-Snail axis could be a cause of resistance of *KRAS* G12C/*LKB1* co-mutated lung cancers to AMG-510. One possible explanation for why KRAS G12C inhibitor treatment upregulated Snail and increased invasion (Supplementary Figure S1I-S1J) is that KRAS G12C inhibition attenuated mTORC1 signaling [102], which may activate autophagy through TFEB dephosphorylation. The upregulation of Snail by AMG-510 treatment was effectively suppressed by the CAMKK2 inhibitor STO-609 (Supplementary Figure S2G), suggesting that inhibition of the autophagy/acetyl-CoA/acetyl-Snail axis could be an effective strategy to prevent resistance to AMG-510 treatment among *KRAS* G12C/*LKB1* co-mutated cancers. Further studies are needed to assess the clinical implications of the proposed strategies.

Among the four KL cell lines used in the study, three cell lines except H157, had the following mutations in *KEAP1*: A549 (G333C), HCC44 (F211C) and H647 (G523W) [103].

The other four K cell lines are *KEAP1* wild-type. Therefore, a limitation of this study was that *LKB1* mutation status in our test panel largely overlapped with *KEAP1* mutation status. As loss-of-function mutation in *KEAP1* is known to promote anti-oxidant gene expression through activation of NRF2, *KEAP1*-mutated cell lines were predicted to have high anti-oxidant gene expression and low mitochondrial ROS levels. However, in this study, we found that KL cell lines had relatively higher mitochondrial ROS levels (Figure 2B) and lower expression of anti-oxidant genes than K cell lines (Supplementary Figure S2B). These data indicated that factors other than *KEAP*1 mutation might affect anti-oxidant gene expression and ROS levels in KL cell lines. We demonstrated that KL context-specific p62 suppression led to impaired anti-oxidant responses, potentially mediated by decreased NRF2 (Figure 2D and Supplementary Figure S2A). One of the possible explanations for these conflicting observations is that *KEAP1* mutations of the corresponding KL cell lines might have a hypomorphic characteristic rather than a complete loss-of-function characteristic, and thus, NRF2 binding to Keap1 might be affected by the levels of p62 and p-p62. Alternatively, *LKB1* loss might involve a Keap1-independent mechanism for impairing NRF2 activity. Further research is needed to fully understand the NRF2 regulatory mechanisms in the context of *LKB1* loss and *KEAP1* mutation.

5 | CONCLUSIONS

In conclusion, cancer cell-intrinsic autophagy driven by ROS-CAMKK2-AMPK in *KRAS-LKB1* co-mutated lung cancer supports tumor invasion and metastasis via Snail acetylation and is further sustained through TFEB acetylation. Targeting the autophagy/acetyl-CoA/acetyl-Snail axis could be a promising treatment strategy for metastatic cancer with activated autophagy.

CONFLICT OF INTERESTS
HSK is a founder and the chief technology officer of Checkmate Therapeutics Inc. MAW is currently an employee of IDEAYA Biosciences Inc. JDM receives licensing fees from the NIH and UTSW for distributing human cell lines.

AUTHOR CONTRIBUTIONS
Conceptualization, HSK, JHH; in vitro experiments, JHH, YKK, SBK, MK, JL, HJY; in vivo experiments, JHH, YKK, MJO; metabolomics and survival data analysis, HK; resources and critical scientific input, KHK, MSL, HJY, JDM, MAW; supervision, HSK; writing, HSK, JHH.

ETHICS APPROVAL AND CONSENT TO PARTICIPATE
All animal procedures for this study were approved by the Institutional Animal Care and Use Committee (IACUC) of Yonsei University.

CONSENT FOR PUBLICATION
Not applicable.

DATA AVAILABILITY STATEMENT
The data that support the findings of this study are available from the corresponding author upon reasonable request.

ORCID
Hyun Seok Kim https://orcid.org/0000-0003-4498-8690

REFERENCES
1. Blandin Knight S, Crosbie PA, Balata H, Chudziak J, Hussell T, Dive C. Progress and prospects of early detection in lung cancer. Open Biol. 2017;7(9).

2. Schabath MB, Cote ML. Cancer progress and priorities: lung cancer. Cancer Epidemiol Biomarkers Prev. 2019;28(10):1563–79.

3. Skoulidis F, Heymach JV. Co-occurring genomic alterations in non-small-cell lung cancer biology and therapy. Nat Rev Cancer. 2019;19(9):495–509.

4. Kim HS, Menditta S, Kim J, Pecot CV, Larsen JE, Zubovych I, et al. Systematic identification of molecular subtype-selective vulnerabilities in non-small-cell lung cancer. Cell. 2013;155(3):552–66.

5. Singh A, Greninger P, Rhodes D, Koopman L, Violette S, Bardeesy N, et al. A gene expression signature associated with "K-Ras addiction" reveals regulators of EMT and tumor cell survival. Cancer Cell. 2009;15(6):489–500.

6. McMillan EA, Ryu MJ, Diep CH, Menditta S, Clemenceau JR, Vaden RM, et al. Chemistry-first approach for nomination of personalized treatment in lung cancer. Cell. 2018;173(4):864–78.e29.

7. Ji H, Ramsey MR, Hayes DN, Fan C, McNamara K, Kozlowski P, et al. LKB1 modulates lung cancer differentiation and metastasis. Nature. 2007;448(7155):807–10.

8. Skoulidis F, Goldberg ME, Greenawalt DM, Hellmann MD, Awad MM, Gainor JF, et al. STK11/LKB1 mutations and PD-1 inhibitor resistance in KRAS-mutant lung adenocarcinoma. Cancer Discov. 2018;8(7):822–35.

9. Mani SA, Guo W, Liao MJ, Eaton EN, Ayyanan A, Zhou AY, et al. The epithelial-mesenchymal transition generates cells with properties of stem cells. Cell. 2008;133(4):704–15.

10. Mowers EE, Sharifi MN, Macleod KF. Autophagy in cancer metastasis. Oncogene. 2017;36(12):1619–30.

11. Gazdar AF, Girard L, Lockwood WW, Lam WL, Minna JD. Lung cancer cell lines as tools for biomedical discovery and research. J Natl Cancer Inst. 2010;102(17):1310–21.

12. Grune T, Kehm R, Hohn A, Jung T. "Cyt/Nuc," a customizable and documenting ImageJ macro for evaluation of protein distributions between cytosol and nucleus. Biotechnol J. 2018;13(5):e1700652.

13. Mizushima N, Yoshimori T, Levine B. Methods in mammalian autophagy research. Cell. 2010;140(3):313–26.

14. Kuo C, Coquoz O, Troy TL, Xu H, Rice BW. Three-dimensional reconstruction of in vivo bioluminescent sources based on multispectral imaging. J Biomed Opt. 2007;12(2): 024007.

15. Kitajima S, Ivanova E, Guo S, Yoshida R, Campisi M, Sundararaman SK, et al. Suppression of STING associated with LKB1 loss in KRAS-driven lung cancer. Cancer Discov. 2019;9(1):34–45.

16. Chen Z, Li JL, Lin S, Cao C, Gimbrone NT, Yang R, et al. cAMP/CREB-regulated LINC00473 marks LKB1-inactivated lung cancer and mediates tumor growth. J Clin Invest. 2016;126(6):2267–79.

17. Beyes S, Andrieux G, Schrempp M, Aicher D, Wenzel J, Anton-Garcia P, et al. Genome-wide mapping of DNA-binding sites identifies stemness-related genes as directly repressed targets of SNAIL1 in colorectal cancer cells. Oncogene. 2019;38(40):6647–61.

18. Wingender E, Dietze P, Karas H, Knuppel R. TRANSFAC: a database on transcription factors and their DNA binding sites. Nucleic Acids Res. 1996;24(1):238–41.

19. Lee KW, Lee NK, Ham S, Roh TY, Kim SH. Twist1 is essential in maintaining mesenchymal state and tumor-initiating properties in synovial sarcoma. Cancer Lett. 2014;343(1):62–73.

20. Cheneby J, Menetrier Z, Mestdagh M, Rosnet T, Douida A, Rhalloussi W, et al. ReMap 2020: a database of regulatory regions from an integrative analysis of Human and Arabidopsis DNA-binding sequencing experiments. Nucleic Acids Res. 2020;48(D1):D180–D8.

21. Barbie DA, Tamayo P, Boehm JS, Kim SY, Moody SE, Dunn IF, et al. Systematic RNA interference reveals that oncogenic KRAS-driven cancers require TBK1. Nature. 2009;462(7269):108–12.

22. Gillette MA, Satpathy S, Cao S, Dhanasekaran SM, Vasaikar SV, Krug K, et al. Proteogenomic characterization reveals therapeutic vulnerabilities in lung adenocarcinoma. Cell. 2020;182(1):200–25.e35.

23. Carretero J, Shimamura T, Rikova K, Jackson AL, Wilkerson MD, Borgman CL, et al. Integrative genomic and proteomic analyses identify targets for Lkb1-deficient metastatic lung tumors. Cancer Cell. 2010;17(6):547–59.

24. Sato M, Larsen JE, Lee W, Sun H, Shames DS, Dalvi MP, et al. Human lung epithelial cells progressed to malignancy through specific oncogenic manipulations. Mol Cancer Res. 2013;11(6):638–50.

25. Sung WJ, Kim H, Park KK. The biological role of epithelial-mesenchymal transition in lung cancer (Review). Oncol Rep. 2016;36(3):1199–206.

26. Batlle E, Sancho E, Franci C, Dominguez D, Monfar M, Baulida J, et al. The transcription factor snail is a repressor of E-cadherin gene expression in epithelial tumour cells. Nat Cell Biol. 2000;2(2):84–9.

27. Chen Z, Cheng K, Walton Z, Wang Y, Ebi H, Shimamura T, et al. A murine lung cancer co-clinical trial identifies genetic modifiers of therapeutic response. Nature. 2012;483(7391): 613–7.

28. Lobb RJ, van Amerongen R, Wiegmans A, Ham S, Larsen JE, Moller A. Exosomes derived from mesenchymal non-small cell lung cancer cells promote chemoresistance. Int J Cancer. 2017;141(3):614–20.

29. Canon J, Rex K, Saiki AY, Mohr C, Cooke K, Bagal D, et al. The clinical KRAS(G12C) inhibitor AMG 510 drives anti-tumour immunity. Nature. 2019;575(7781):217–23.

30. Faubert B, Vincent EE, Griss T, Samborska B, Izreig S, Svensson RU, et al. Loss of the tumor suppressor LKB1 promotes metabolic reprogramming of cancer cells via HIF-1alpha. Proc Natl Acad Sci USA. 2014;111(7):2554–9.

31. Shackelford DB, Abt E, Gerken L, Vasquez DS, Seki A, Leblanc M, et al. LKB1 inactivation dictates therapeutic response of non-small cell lung cancer to the metabolism drug phenformin. Cancer Cell. 2013;23(2):143–58.

32. Xu HG, Zhai YX, Chen J, Lu Y, Wang JW, Quan CS, et al. LKB1 reduces ROS-mediated cell damage via activation of p38. Oncogene. 2015;34(29):3848–59.

33. Taguchi K, Fujikawa N, Komatsu M, Ishii T, Unno M, Akaike T, et al. Keap1 degradation by autophagy for the maintenance of redox homeostasis. Proc Natl Acad Sci USA. 2012;109(34): 13561–6.

34. Komatsu M, Kurokawa H, Waguri S, Taguchi K, Kobayashi A, Ichimura Y, et al. The selective autophagy substrate p62

activates the stress responsive transcription factor Nrf2 through inactivation of Keap1. Nat Cell Biol. 2010;12(3):213–23.

35. Bae SH, Sung SH, Oh SY, Lim JM, Lee SK, Park YN, et al. Sestrins activate Nrf2 by promoting p62-dependent autophagic degradation of Keap1 and prevent oxidative liver damage. Cell Metab. 2013;17(1):73–84.

36. Rabinovitch RC, Samborska B, Faubert B, Ma EH, Gravel SP, Andrzejewski S, et al. AMPK maintains cellular metabolic homeostasis through regulation of mitochondrial reactive oxygen species. Cell Rep. 2017;21(1):1–9.

37. Garcia D, Shaw RJ. AMPK: mechanisms of cellular energy sensing and restoration of metabolic balance. Mol Cell. 2017;66(6):789–800.

38. Shackelford DB, Shaw RJ. The LKB1-AMPK pathway: metabolism and growth control in tumour suppression. Nat Rev Cancer. 2009;9(8):563–75.

39. Hardie DG, Ross FA, Hawley SA. AMPK: a nutrient and energy sensor that maintains energy homeostasis. Nat Rev Mol Cell Biol. 2012;13(4):251–62.

40. Hudmon A, Schulman H. Structure-function of the multifunctional Ca2+/calmodulin-dependent protein kinase II. Biochem J. 2002;364(Pt 3):593–611.

41. Mihaylova MM, Shaw RJ. The AMPK signalling pathway coordinates cell growth, autophagy and metabolism. Nat Cell Biol. 2011;13(9):1016–23.

42. Sardiello M, Palmieri M, di Ronza A, Medina DL, Valenza M, Gennarino VA, et al. A gene network regulating lysosomal biogenesis and function. Science. 2009;325(5939):473–7.

43. Palmieri M, Impey S, Kang H, di Ronza A, Pelz C, Sardiello M, et al. Characterization of the CLEAR network reveals an integrated control of cellular clearance pathways. Hum Mol Genet. 2011;20(19):3852–66.

44. Roczniak-Ferguson A, Petit CS, Froehlich F, Qian S, Ky J, Angarola B, et al. The transcription factor TFEB links mTORC1 signaling to transcriptional control of lysosome homeostasis. Sci Signal. 2012;5(228):ra42.

45. Doble BW, Woodgett JR. Role of glycogen synthase kinase-3 in cell fate and epithelial-mesenchymal transitions. Cells Tissues Organs. 2007;185(1-3):73–84.

46. Doble BW, Woodgett JR. GSK-3: tricks of the trade for a multi-tasking kinase. J Cell Sci. 2003;116(Pt 7):1175–86.

47. Li H, Ning S, Ghandi M, Kryukov GV, Gopal S, Deik A, et al. The landscape of cancer cell line metabolism. Nat Med. 2019;25(5):850–60.

48. Yu G, Cheng CJ, Lin SC, Lee YC, Frigo DE, Yu-Lee LY, et al. Organelle-derived acetyl-CoA promotes prostate cancer cell survival, migration, and metastasis via activation of calmodulin kinase II. Cancer Res. 2018;78(10):2490–502.

49. Rios Garcia M, Steinbauer B, Srivastava K, Singhal M, Mattijssen F, Maida A, et al. Acetyl-CoA carboxylase 1-dependent protein acetylation controls breast cancer metastasis and recurrence. Cell Metab. 2017;26(6):842–55.e5.

50. Lu M, Zhu WW, Wang X, Tang JJ, Zhang KL, Yu GY, et al. ACOT12-dependent alteration of acetyl-CoA drives hepatocellular carcinoma metastasis by epigenetic induction of epithelial-mesenchymal transition. Cell Metab. 2019;29(4):886–900.e5.

51. Fendt SM, Bell EL, Keibler MA, Olenchock BA, Mayers JR, Wasylenko TM, et al. Reductive glutamine metabolism is a function of the alpha-ketoglutarate to citrate ratio in cells. Nat Commun. 2013;4:2236.

52. Lee WD, Mukha D, Aizenshtein E, Shlomi T. Spatial-fluxomics provides a subcellular-compartmentalized view of reductive glutamine metabolism in cancer cells. Nat Commun. 2019;10(1):1351.

53. Dancy BM, Cole PA. Protein lysine acetylation by p300/CBP. Chem Rev. 2015;115(6):2419–52.

54. Wellen KE, Hatzivassiliou G, Sachdeva UM, Bui TV, Cross JR, Thompson CB. ATP-citrate lyase links cellular metabolism to histone acetylation. Science. 2009;324(5930):1076–80.

55. Hsu DS, Wang HJ, Tai SK, Chou CH, Hsieh CH, Chiu PH, et al. Acetylation of snail modulates the cytokinome of cancer cells to enhance the recruitment of macrophages. Cancer Cell. 2014;26(4):534–48.

56. Settembre C, Di Malta C, Polito VA, Garcia Arencibia M, Vetrini F, Erdin S, et al. TFEB links autophagy to lysosomal biogenesis. Science. 2011;332(6036):1429–33.

57. Settembre C, Zoncu R, Medina DL, Vetrini F, Erdin S, Erdin S, et al. A lysosome-to-nucleus signalling mechanism senses and regulates the lysosome via mTOR and TFEB. EMBO J. 2012;31(5):1095–108.

58. Wang C, Niederstrasser H, Douglas PM, Lin R, Jaramillo J, Li Y, et al. Small-molecule TFEB pathway agonists that ameliorate metabolic syndrome in mice and extend C. elegans lifespan. Nat Commun. 2017;8(1):2270.

59. Commisso C, Davidson SM, Soydaner-Azeloglu RG, Parker SJ, Kamphorst JJ, Hackett S, et al. Macropinocytosis of protein is an amino acid supply route in Ras-transformed cells. Nature. 2013;497(7451):633–7.

60. Eskelinen EL, Illert AL, Tanaka Y, Schwarzmann G, Blanz J, Von Figura K, et al. Role of LAMP-2 in lysosome biogenesis and autophagy. Mol Biol Cell. 2002;13(9):3355–68.

61. Galdieri L, Zhang T, Rogerson D, Lleshi R, Vancura A. Protein acetylation and acetyl coenzyme a metabolism in budding yeast. Eukaryot Cell. 2014;13(12):1472–83.

62. Nakano T, Kanai Y, Amano Y, Yoshimoto T, Matsubara D, Shibano T, et al. Establishment of highly metastatic KRAS mutant lung cancer cell sublines in long-term three-dimensional low attachment cultures. PLoS One. 2017;12(8):e0181342.

63. Yang S, Wang X, Contino G, Liesa M, Sahin E, Ying H, et al. Pancreatic cancers require autophagy for tumor growth. Genes Dev. 2011;25(7):717–29.

64. Peng YF, Shi YH, Ding ZB, Ke AW, Gu CY, Hui B, et al. Autophagy inhibition suppresses pulmonary metastasis of HCC in mice via impairing anoikis resistance and colonization of HCC cells. Autophagy. 2013;9(12):2056–68.

65. Lazova R, Camp RL, Klump V, Siddiqui SF, Amaravadi RK, Pawelek JM. Punctate LC3B expression is a common feature of solid tumors and associated with proliferation, metastasis, and poor outcome. Clin Cancer Res. 2012;18(2):370–9.

66. Zhao H, Yang M, Zhao J, Wang J, Zhang Y, Zhang Q. High expression of LC3B is associated with progression and poor outcome in triple-negative breast cancer. Med Oncol. 2013;30(1):475.

67. Han C, Sun B, Wang W, Cai W, Lou D, Sun Y, et al. Overexpression of microtubule-associated protein-1 light chain 3

is associated with melanoma metastasis and vasculogenic mimicry. Tohoku J Exp Med. 2011;223(4):243–51.

68. Galavotti S, Bartesaghi S, Faccenda D, Shaked-Rabi M, Sanzone S, McEvoy A, et al. The autophagy-associated factors DRAM1 and p62 regulate cell migration and invasion in glioblastoma stem cells. Oncogene. 2013;32(6):699–712.

69. Benzarti M, Delbrouck C, Neises L, Kiweler N, Meiser J. Metabolic potential of cancer cells in context of the metastatic cascade. Cells. 2020;9(9).

70. Thirupathi A, Chang YZ. Role of AMPK and its molecular intermediates in subjugating cancer survival mechanism. Life Sci. 2019;227:30–8.

71. Li J, Yang B, Zhou Q, Wu Y, Shang D, Guo Y, et al. Autophagy promotes hepatocellular carcinoma cell invasion through activation of epithelial-mesenchymal transition. Carcinogenesis. 2013;34(6):1343–51.

72. Lock R, Kenific CM, Leidal AM, Salas E, Debnath J. Autophagy-dependent production of secreted factors facilitates oncogenic RAS-driven invasion. Cancer Discov. 2014;4(4):466–79.

73. Yamamoto K, Venida A, Yano J, Biancur DE, Kakiuchi M, Gupta S, et al. Autophagy promotes immune evasion of pancreatic cancer by degrading MHC-I. Nature. 2020;581(7806): 100–5.

74. Jung HY, Fattet L, Tsai JH, Kajimoto T, Chang Q, Newton AC, et al. Apical-basal polarity inhibits epithelial-mesenchymal transition and tumour metastasis by PAR-complex-mediated SNAI1 degradation. Nat Cell Biol. 2019;21(3):359–71.

75. Li CF, Chen JY, Ho YH, Hsu WH, Wu LC, Lan HY, et al. Snail-induced claudin-11 prompts collective migration for tumour progression. Nat Cell Biol. 2019;21(2):251–62.

76. Zhao GX, Xu YY, Weng SQ, Zhang S, Chen Y, Shen XZ, et al. CAPS1 promotes colorectal cancer metastasis via Snail mediated epithelial mesenchymal transformation. Oncogene. 2019;38(23):4574–89.

77. Dong C, Yuan T, Wu Y, Wang Y, Fan TW, Miriyala S, et al. Loss of FBP1 by Snail-mediated repression provides metabolic advantages in basal-like breast cancer. Cancer Cell. 2013;23(3):316–31.

78. Kudo-Saito C, Shirako H, Takeuchi T, Kawakami Y. Cancer metastasis is accelerated through immunosuppression during Snail-induced EMT of cancer cells. Cancer Cell. 2009;15(3):195–206.

79. Moody SE, Perez D, Pan TC, Sarkisian CJ, Portocarrero CP, Sterner CJ, et al. The transcriptional repressor Snail promotes mammary tumor recurrence. Cancer Cell. 2005;8(3):197–209.

80. Barrallo-Gimeno A, Nieto MA. The Snail genes as inducers of cell movement and survival: implications in development and cancer. Development. 2005;132(14):3151–61.

81. Zhou BP, Deng J, Xia W, Xu J, Li YM, Gunduz M, et al. Dual regulation of Snail by GSK-3beta-mediated phosphorylation in control of epithelial-mesenchymal transition. Nat Cell Biol. 2004;6(10):931–40.

82. Zheng H, Shen M, Zha YL, Li W, Wei Y, Blanco MA, et al. PKD1 phosphorylation-dependent degradation of SNAIL by SCF-FBXO11 regulates epithelial-mesenchymal transition and metastasis. Cancer Cell. 2014;26(3):358–73.

83. Vinas-Castells R, Beltran M, Valls G, Gomez I, Garcia JM, Montserrat-Sentis B, et al. The hypoxia-controlled FBXL14

ubiquitin ligase targets SNAIL1 for proteasome degradation. J Biol Chem. 2010;285(6):3794–805.

84. Qin ZY, Wang T, Su S, Shen LT, Zhu GX, Liu Q, et al. BRD4 promotes gastric cancer progression and metastasis through acetylation-dependent stabilization of snail. Cancer Res. 2019;79(19):4869–81.

85. Gomes LC, Di Benedetto G, Scorrano L. During autophagy mitochondria elongate, are spared from degradation and sustain cell viability. Nat Cell Biol. 2011;13(5):589–98.

86. Graef M, Nunnari J. Mitochondria regulate autophagy by conserved signalling pathways. EMBO J. 2011;30(11):2101–14.

87. Toyama EQ, Herzig S, Courchet J, Lewis TL, Jr, Loson OC, Hellberg K, et al. Metabolism. AMP-activated protein kinase mediates mitochondrial fission in response to energy stress. Science. 2016;351(6270):275–81.

88. Deus CM, Yambire KF, Oliveira PJ, Raimundo N. Mitochondria-lysosome crosstalk: from physiology to neurodegeneration. Trends Mol Med. 2020;26(1):71–88.

89. Zhang J, Wang J, Zhou Z, Park JE, Wang L, Wu S, et al. Importance of TFEB acetylation in control of its transcriptional activity and lysosomal function in response to histone deacetylase inhibitors. Autophagy. 2018;14(6):1043–59.

90. Sha Y, Rao L, Settembre C, Ballabio A, Eissa NT. STUB1 regulates TFEB-induced autophagy-lysosome pathway. EMBO J. 2017;36(17):2544–52.

91. Ettinger DS, Wood DE, Aggarwal C, Aisner DL, Akerley W, Bauman JR, et al. NCCN guidelines insights: non-small cell lung cancer, version 1.2020. J Natl Compr Canc Netw. 2019;17(12):1464–72.

92. Mazieres J, Drilon A, Lusque A, Mhanna L, Cortot AB, Mezquita L, et al. Immune checkpoint inhibitors for patients with advanced lung cancer and oncogenic driver alterations: results from the IMMUNOTARGET registry. Ann Oncol. 2019;30(8):1321–8.

93. Ageta-Ishihara N, Takemoto-Kimura S, Nonaka M, Adachi-Morishima A, Suzuki K, Kamijo S, et al. Control of cortical axon elongation by a GABA-driven Ca2+/calmodulin-dependent protein kinase cascade. J Neurosci. 2009;29(43):13720–9.

94. Cary RL, Waddell S, Racioppi L, Long F, Novack DV, Voor MJ, et al. Inhibition of Ca(2)(+)/calmodulin-dependent protein kinase kinase 2 stimulates osteoblast formation and inhibits osteoclast differentiation. J Bone Miner Res. 2013;28(7):1599–610.

95. O'Byrne SN, Scott JW, Pilotte JR, Santiago ADS, Langendorf CG, Oakhill JS, et al. In depth analysis of kinase cross screening data to identify CAMKK2 inhibitory scaffolds. Molecules. 2020;25(2).

96. York B, Li F, Lin F, Marcelo KL, Mao J, Dean A, et al. Pharmacological inhibition of CaMKK2 with the selective antagonist STO-609 regresses NAFLD. Sci Rep. 2017;7(1):11793.

97. Racioppi L, Nelson ER, Huang W, Mukherjee D, Lawrence SA, Lento W, et al. CaMKK2 in myeloid cells is a key regulator of the immune-suppressive microenvironment in breast cancer. Nat Commun. 2019;10(1):2450.

98. Dower CM, Wills CA, Frisch SM, Wang HG. Mechanisms and context underlying the role of autophagy in cancer metastasis. Autophagy. 2018;14(7):1110–28.

99. van Staalduinen J, Baker D, Ten Dijke P, van Dam H. Epithelial-mesenchymal-transition-inducing transcription factors: new

targets for tackling chemoresistance in cancer? Oncogene. 2018;37(48):6195–211.

100. Hata AN, Shaw AT. Resistance looms for KRAS(G12C) inhibitors. Nat Med. 2020;26(2):169–70.

101. Adachi Y, Ito K, Hayashi Y, Kimura R, Tan TZ, Yamaguchi R, et al. Epithelial-to-mesenchymal transition is a cause of both intrinsic and acquired resistance to KRAS G12C inhibitor in KRAS G12C-mutant non-small cell lung cancer. Clin Cancer Res. 2020;26(22):5962–73.

102. Bar-Sagi D, Knelson EH, Sequist LV. A bright future for KRAS inhibitors. Nature Cancer. 2020;1(1):25–7.

103. Goldstein LD, Lee J, Gnad F, Klijn C, Schaub A, Reeder J, et al. Recurrent loss of NFE2L2 exon 2 is a mechanism for Nrf2 pathway activation in human cancers. Cell Rep. 2016;16(10):2605–17.

SUPPORTING INFORMATION

Additional supporting information can be found online in the Supporting Information section at the end of this article.